Journal of Computing & Biomedical Informatics
ISSN: 2710 - 1606

Volume 10 Issue 01
2025

Research Article
https://doi.org/10.56979/1001/2025/1142

Lung Tumor Detection using LW-convMLP Segmentation with Improved Golden Jackal Optimization-based DRNet-MM Classification

Suma K G[1], Santhi Gottumukkala[2], Archana Sasi[3], Santhi Sri T[4], Ghamya Kotapati[5], Ramesh Vatambeti[6*], and Rama Ganesh B[7]

[1]School of Computer Science and Engineering, VIT-AP University, Vijayawada, India.
[2]Department of Mathematics, S.R.K.R. Engineering College, Bhimavaram, India.
[3]Department of CSE, Faculty of Engineering and Technology, Jain University, Kannagapura Rd, Bengaluru, Karnataka 562112, India.
[4]Department of Computer Science and Engineering, Koneru Lakshmaiah Education Foundation, Vaddeswaram, India.
[5]School of Computing, Mohan Babu University, Tirupati, India.
[6]Department of CSE, Tezpur University, Tezpur 784028, Assam, India.
[7]Department of Computer Science and Engineering, Sri Venkatesa Perumal College of Engineering & Technology, Puttur 517583, India.
[*]Corresponding Author: Ramesh Vatambeti. E-Mail: v2ramesh634@gmail.com

Received: September 13, 2025 **Accepted:** November 22, 2025

Abstract: Lung cancer (LC) remains a critical global health issue, characterized by abnormal cell proliferation. Early detection is crucial, relying on imaging techniques such as CT, MRI, and ultrasound. This study leverages the Linear Imaging and Self-Scanning Sensor (LISS) and the Lung Image Database Consortium and Image Database Resource Initiative (LIDC-IDRI) datasets. CT images were pre-processed using local fractional entropy (LFE) and rolling guidance filtering (RGF). Tumor segmentation was performed using the Light Weight Medical Image Segmentation Network, integrating Convolutional Neural Network (CNN) and Multi-Layered Perceptron (MLP) based on the UNet architecture (LW-convMLP UNet). The study assessed the efficacy of the Deep Residual Neural Network with Masked Modeling (DRNet-MM) for LC classification, with hyperparameters optimized using the Improved Golden Jackal Optimization Algorithm (IGJOA). The proposed model exhibited outstanding performance, achieving precision and accuracy scores of 99.10% and 99.4% for LIDC-IDRI, and 90.3% and 90.25% for LISS. In conclusion, this method surpasses previous approaches, demonstrating its effectiveness in detecting and categorizing lung tumors.

Keywords: Lung Cancer Detection; Convolutional Neural Networks; Rolling Guidance Filtering; Local Fractional Entropy; Improved Golden Jackal Optimization

1. Introduction

Owing to a notable surge in documented cases in recent years, cancer has become a major global cause of death. According to the most recent data obtained from Global Cancer Statistics (GLOBOCAN) [1], there were roughly 19.3 million additional instances of cancer diagnosed worldwide in a single year, leading to the unfortunate deaths of 9.96 million people in 2020 alone. Cancer, one of the deadliest illnesses of the modern era, poses a serious risk to human life. In fact, according to WHO projections, cancer was expected to be the leading cause of death worldwide in 2020 [2].

Particularly, lung cancer (LC) has proven to be a dangerous adversary, accounting for approximately 1.80 million cancer-related deaths globally. It is alarming to note that by 2035, cancer-related deaths could rise by as much as 60% [3]. LC is primarily associated with smoking and is still prevalent or on the rise in several nations. It is characterized by irregular cells growing out of control in the lung tissues [4], suggesting that LC cases should rise even further in the next few decades [5]. However, studies, as reported by Dubin et al. [6], have demonstrated that LC can also affect non-smokers due to reasons such as pre-existing lung conditions, genetic predisposition, occupational hazards, and environmental pollutants.

Computed Tomography (CT) has become the gold standard in medical imaging for identifying and evaluating lung tumors. Accurately identifying carcinogenic tumors from CT scan imaging is essential for early LC detection, improving the prognosis for patients. For healthcare practitioners, this crucial procedure provides essential information [7-8].

Malignant (cancerous) and benign (non-cancerous) lung tumors are typically divided into two categories, even though they frequently present with nonspecific symptoms [9]. Determining whether a lung tumor is benign or malignant is a crucial step after a patient is diagnosed. One characteristic of benign tumors is their slow, noncancerous growth. Benign tumor cells do not invade neighbouring tissues; instead, they remain contained within the tumor's boundaries [10]. While benign tumors rarely cause significant harm, they can occasionally develop into large masses with distinct borders.

On the other hand, malignant tumors are cancerous and have the potential to spread through the lymphatic or circulatory systems to other areas of the body [11]. These tumors lack distinct borders and easily invade nearby cells. Malignant tumors can proliferate quickly, and even after surgical removal, they may tend to return. Figure 1, annotated for clarity, provides a visual representation of the difference between benign and malignant tumors. Figure 1a illustrates a benign tumor; Figure 1b depicts a malignant tumor discovered during a lung CT scan, and Figure 1c shows a typical lung CT image.

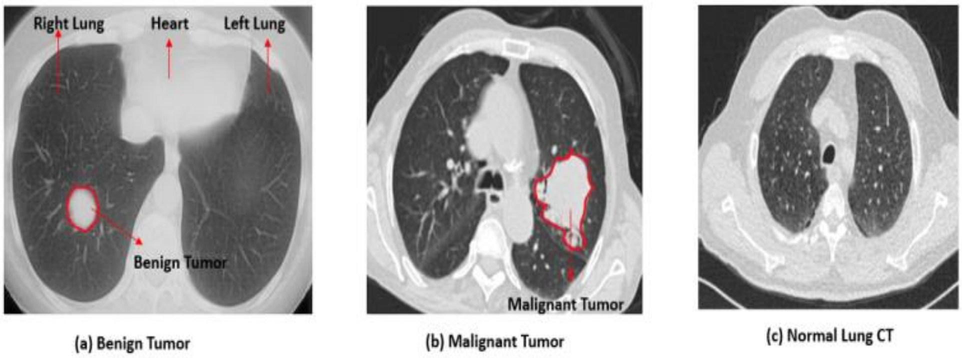

(a) Benign Tumor (b) Malignant Tumor (c) Normal Lung CT

Figure 1. Illustration of lung lesion malignancy

John McCarthy initially used the term "artificial intelligence," or AI, in 1956. It alludes to using technology and computers to mimic human-like intelligent thought and problem-solving [12]. This technology can potentially make significant advancements in several medical fields, such as diagnosis, treatment management, and treatment outcome prediction, due to its capacity to analyse and interpret complex data [13].

As a branch of artificial intelligence, deep learning (DL) aims to mimic human cognitive processes to acquire knowledge. It excels at tasks like image segmentation, classification, and object detection, and is a useful tool for processing large amounts of medical data due to its exceptional performance and versatility [14]. CNN is one particular DL method utilized for image recognition. Due to its skill at accurately identifying complex feature representations, CNN is widely used in image processing. By directly extracting multi-layered features from the data, CNN has been the cornerstone of this technology's achievements in several biological domains.

Even though segmentation can be challenging, it is crucial in medical imaging. Manual segmentation requires much work and may result in discrepancies between individuals. CNN-based segmentation, on the other hand, is more accurate and efficient [15]. Medical imaging frequently involves classification tasks, such as classifying images of lung cancer (LC). By providing medical professionals with insightful information, these classification missions aid in diagnosis and improve the speed and precision of clinical diagnosis [16].

Lung cancer (LC) continues to be a major worldwide public health issue, affecting millions. Reducing mortality rates and improving patient outcomes directly relate to timely detection and diagnosis. Even though CT is the most popular technique for diagnosing lung tumors, there are image interpretation issues that could result in misinterpretations. To tackle these issues and improve the precision of LC diagnosis, a novel DL-based CT image classification technique has been proposed.

The main goal of this research is to build a strong and dependable model that can analyse CT scans on its own and accurately distinguish between benign and malignant lung tumors. The ultimate objective of this project is to significantly increase the accuracy and effectiveness of CT image interpretation, enabling earlier diagnoses and better patient outcomes. The study aims to support the ongoing fight against LC by developing this cutting-edge DL-based classification method for LC detection, benefiting both patients and medical professionals.

The major contributions of this study are summarized as follows:

- **A modified LW-convMLP UNet segmentation architecture** is introduced, incorporating (i) dual-stage LDA modules with asymmetric/depth wise separable convolution, and (ii) a lightweight LMLP block that performs horizontal–vertical MLP tokenization followed by deep convolutional refinement. These architectural elements are specifically designed to reduce computational load while improving boundary-aware tumor segmentation—features not present in prior CNN-MLP hybrid UNet variants.
- **A DRNet-MM classification module** is formulated by embedding a complex-valued residual encoder with a targeted masked-modeling (MM) reconstruction strategy. Unlike traditional autoencoder-based classifiers, DRNet-MM forces the network to infer missing lung regions, thereby strengthening tumor-relevant latent representations and improving robustness under limited data scenarios.
- **An Improved Golden Jackal Optimization (IGJO) strategy** is developed by integrating Rosenbrock's rotational direct search with the original GJO mechanism. This modification enhances the balance between exploration and exploitation and is used—uniquely in this work—to optimize DRNet-MM hyperparameters, significantly reducing sensitivity to manual tuning.
- **A unified segmentation–classification pipeline** is constructed, wherein the LW-convMLP UNet provides precise tumor masks that guide the DRNet-MM classifier. This sequential integration improves stability in end-to-end inference and is empirically shown to outperform conventional setups where segmentation and classification operate independently.
- **Comprehensive evaluation on two heterogeneous datasets (LISS and LIDC-IDRI)** demonstrates the superior generalization of the proposed framework across varying imaging conditions. All preprocessing, training, and hyperparameter settings are reported explicitly to enhance reproducibility and facilitate future benchmarking.

Unlike generic CNN–MLP combinations or standard metaheuristic tuning, our work contributes architectural modifications and an improved optimization scheme tailored specifically to lung tumor analysis. Each component is designed to address a distinct challenge—noise-sensitive CT segmentation, limited annotated samples, and unstable hyperparameter sensitivity. These innovations collectively distinguish the proposed model from existing deep learning pipelines.

The paper is organised as follows: Section 1 introduces the history, subtypes, DL, and problem statement of LC. Section 2 provides an analysis of current models with problem declarations. A brief synopsis of the anticipated model is provided in Sections 3 and 4. Section 5 presents the experimental comparability of the suggested design with the existing models. Section 6 offers the conclusion and suggestions for additional research.

2. Related Work

The research conducted by Tyagi et al. [17] aimed to create an efficient system for classifying lung cancer (LC) stages based on TNM guidelines. They introduced the LC Stage Classification Network (LCSCNet), a multi-level 3D deep Convolutional Neural Network (CNN). LCSCNet utilized three different classifier networks to classify the T, N, and M labels. Data pre-processing, including label file processing and CT image augmentation, was performed to obtain TNM labels. LCSCNet employed a dense CNN with asymmetric convolution and a simultaneous squeeze and excitation module as an independent classification technique for each label. The combined results determined the final stage classification, with the simultaneous squeeze and excitation module improving performance by emphasizing important image information. Asymmetric convolution was included for computational efficiency. The study achieved remarkable average accuracies for T-Stage, N-Stage, and M-Stage (97.63%, 97.63%, and 96.92%, respectively) using two publicly available datasets, resulting in an overall stage classification accuracy of 97%.

In another study, Irshad et al. [18] presented an Internet of Things (IoT)-enabled healthcare monitoring system for LC detection. They introduced an Improved Grey Wolf Optimization (IGWO) deep CNN model along with the Grey Wolf Optimization (GWO) method. The Tasmanian Devil Optimization (TDO) algorithm was integrated to improve the convergence rate of GWO and find relevant features for lung nodule diagnosis. The IGWO-based DCNN model utilized valuable features from the IoT platform and stored outcomes in cloud storage for professional analysis. The Android operating system and Python libraries were used for implementation. Their method, incorporating GWO and IoT, outperformed recent models for LC detection.

Sun et al. [19] investigated the potential of the Swin Transformer model for LC segmentation and classification. The pre-trained Swin-B model outperformed ViT in the classification task, achieving a top-1 accuracy of 82.26%. The Swin-S model excelled in the segmentation task, particularly in mean Intersection over Union (mIoU). Pre-training enhanced the Swin Transformer model's performance on these specific tasks.

Appadurai et al. [20] proposed a novel model for the precise extraction of lung nodules from 3D CT scans. They employed two crucial pre-processing steps, utilizing the Markov-Gibbs random field (MGRF) model to differentiate lung wall nodules and a DL U-net technique for nodule segmentation. To address segmentation challenges, a 3D U-net trained with a specific loss function was employed. The segmentation method demonstrated superiority over advanced deep learning techniques in distinguishing lung nodules.

Siddique et al. [21] aimed to improve lung CT image classification with a focus on processing time and early cancer detection. They introduced a new technique incorporating Gaussian-Bernoulli (GB) and Bernoulli-Bernoulli (BB) restricted Boltzmann machines in an enhanced Deep Belief Network (E-DBN). The support vector machine (SVM) proved to be the most accurate technique, markedly improving multiple performance metrics. The proposed model was evaluated using the publicly available LUNA-16 and LIDC-IDRI datasets.

Subashchandrabose et al. [22] presented a novel method for multi-level LC classification using an ensemble Federated Learning framework. To enhance accuracy and generalization while adhering to privacy and data security regulations, multiple machine learning models trained on various datasets were combined. Their approach achieved an impressive 89.63% accuracy in classifying LC when tested on a Kaggle cancer dataset.

Usman and Shin [23] proposed a two-phase method for segmenting three-dimensional lung nodules. They utilized a dual-encoder-based hard attention network (DEHA-Net) for segmenting lung nodules in axial slices and creating ROI masks for neighbouring slices using an adaptive region of interest (A-ROI) algorithm. Their method demonstrated enhanced robustness, outperforming recent approaches with an average Dice similarity coefficient (DSC) of 87.91%, sensitivity (SEN) of 90.84%, and positive predictive value of 89.56%.

Said et al. [24] developed a comprehensive system for early LC diagnosis using self-supervised and UNETR network segmentation. Their method classified segmented regions as benign or malignant, achieving a classification accuracy of 98.77% and a segmentation accuracy of 97.83% on the Decathlon dataset. This 3D-input CT scan-based approach provided a reliable tool for early LC diagnosis and treatment.

Ji et al. [25] introduced the ELCT-YOLO model to address the scaling problem and enable real-time identification of lung tumors in CT images. The model, featuring a specially constructed neck structure and a cascaded refinement scheme (CRS), excelled in identifying lung tumors of different sizes.

Zhang et al. [26] aimed to increase the accuracy of lung nodule CT image segmentation using U-Net. They incorporated a local residual design for up sampling, dense network connections, and a sawtooth expanded Conv design. The suggested algorithm demonstrated improvements in accuracy and performance under different loss functions compared to the original U-Net segmentation method.

Lanjewar et al. [27] classified LC into various groups using a dataset of chest CT scan images from Kaggle. They employed a state-of-the-art deep learning method, feeding different machine learning classifiers with DenseNet201 features. Their system's exceptional performance and high accuracy highlighted the potential of machine learning and computer technology in CT scan-based LC diagnosis.

Shah et al. [28] utilized CNNs to recognize potentially malignant lung nodules in CT scan images. They employed an ensemble strategy, combining multiple CNNs to improve detection precision. The combined accuracy of 95% demonstrated the superior performance of their Deep Ensemble 2D CNN compared to the baseline technique.

Maleki and Niaki [29] investigated three different CT image processing methods for LC diagnosis, including CNN, feature extraction techniques, pre-processing, and image segmentation. They employed Random Forest (RF), Gradient Boosting (GB), and Support Vector Machine (SVM) classification techniques, achieving a respectable accuracy rate of 95% for LC diagnosis.

Bishnoi and Goel [30] presented a high-speed real-time transfer learning framework for differentiating between benign and malignant LC slices in CT scans. The framework utilized K-means clustering for segmentation and pre-processing, Nvidia Tensor-RT for real-time deployment, and a weighted VGG deep network (WVDN) model for tuning and regularization. With an F1 score of 0.93, a Cohen's kappa score of 0.85, and statistical analysis results of 93.2% accuracy, precision, and recall, their model demonstrated superior performance, representing a significant breakthrough in clinical diagnosis based on whole CT slices.

2.1. Research Gap

Despite significant progress in deep learning-based lung cancer CAD systems, several key limitations remain. Most existing methods rely on heavy segmentation or classification backbones that are difficult to deploy in resource-constrained clinical environments. Many systems treat segmentation and classification as separate tasks, resulting in information loss between stages and reduced diagnostic reliability. Moreover, few approaches demonstrate robust performance across heterogeneous datasets, and hyperparameters are often tuned manually rather than through principled optimization, leading to inconsistent results and limited reproducibility.

To address these gaps, our framework introduces a lightweight yet expressive LW-convMLP UNet for efficient tumor segmentation, integrates a robust DRNet-MM classifier to improve malignancy discrimination, and employs an Improved Golden Jackal Optimization (IGJO) strategy for systematic hyperparameter search. This design enables a unified, computationally efficient, and cross-dataset generalizable solution for benign–malignant lung tumor differentiation.

3. Materials

Figure 2 depicts the flow of the suggested approach's steps. The initial step is preprocessing, which is followed by tumor segmentation, classification, and hyperparameter tuning for the classification model.

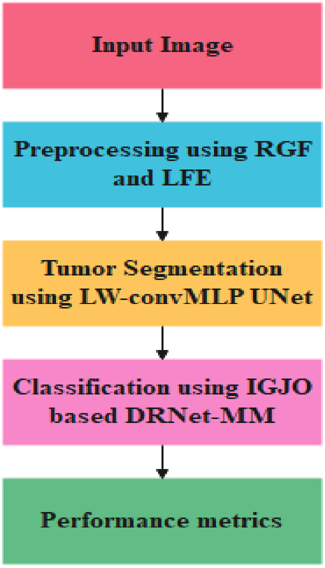

Figure 2. Flowchart of the work.

3.1. Dataset description

(i) LISS Dataset

The LISS Dataset, officially known as LISS CISL (A Public Database of Common Imaging Signs of Lung Diseases), was accessed on October 19, 2022. This dataset is now available to the public for educational and scientific purposes. It comprises 511 2D Common Imaging Signs of Lung Diseases (CISLs) from 252 patients and 166 3D images from 19 patients. These images showcase nearly nine different lung nodule symptoms and were captured at the Cancer Institute and Hospital of the Chinese Academy of Medical Sciences, utilizing two CT scanners from Holt, Michigan, USA: the Toshiba Aquilion 64 Slice and the GELightSpeed VCT 64. All images adhere to DICOM 3.0 requirements. The dataset includes three-dimensional examples of lung nodule signs, focusing on "ground glass opacity (GGO)," while the 2D data in the LISS database is categorized into nine distinct types [31]. Figure 3 in the dataset illustrates the locations of each of the nine lung nodule indicators in the images.

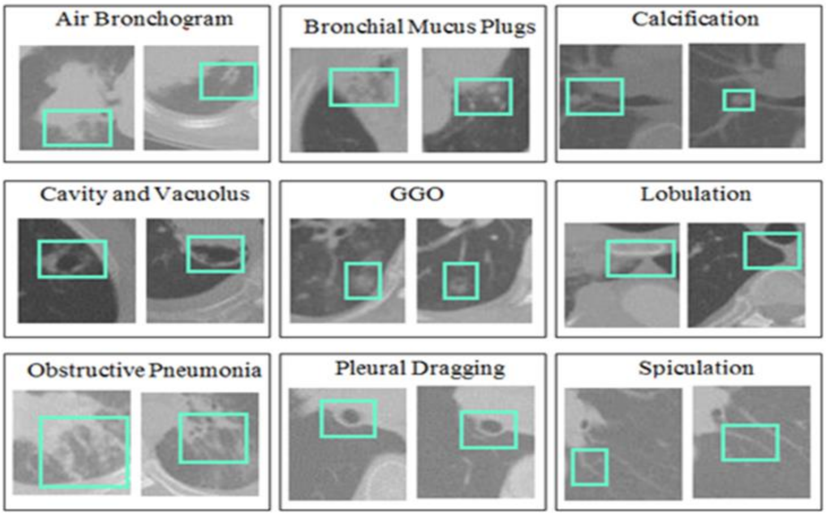

Figure 3. Abnormal Signs in LISS Dataset

(ii) LIDC-IDRI Dataset

The LIDC IDRI dataset stands as the largest publicly available resource for researchers worldwide [32]. Illustrated in Figure 4(a–d), this collection comprises 1018 CT scan images of the thoracic region from 1010 different patients. Figures 4(a)–(d) respectively show the CT slices with annotations, benign and malignant nodule examples, and segmentation boundaries used in classification. These images include valuable annotations in the form of nodule outlines, aiding in the detection of lung cancers. It is noteworthy that all patients in the dataset have access to nodule annotations. However, comprehensive diagnostic data is available only for 157 of these patients. Nodule information ratings are part of the diagnostic data and are categorized as follows: 0 signifies an unknown classification, 1 indicates a benign class, 2 denotes a primary malignancy class, and 3 represents a metastatic (malignancy) class.

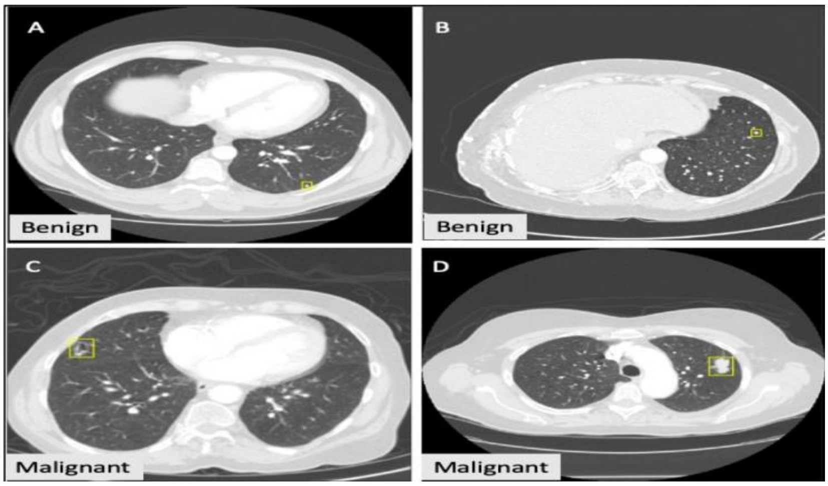

Figure 4. Lung classification results

A comprehensive assessment, encompassing data on disease progression, surgical resection findings, biopsy results, and a detailed examination of radiological images, is employed to determine image ratings. The diagnostic classification comprises two separate categories: (i) patient-level assessment and (ii) tumor-level evaluation. This specialized dataset consists of images from a cohort of one thousand patients, designed to support radiologists. The images were captured using various CT scanning equipment over an extended period. Table 1 displays the distribution of nodule diameters according to the LIDC IDRI database, which contains numerous lung nodules spread across various image slices. Annotated data are present in every slice showing a lung nodule, and the presence of these nodules is determined by a 3 mm size criterion.

Table 1. Description of the LIDC IDRI Dataset

Nodule Description	No. of nodules
No. of <3 mm nodules marked by all 4 radiologist	928
No. of <3 mm nodules marked by at least 1 radiologist	2669
No. of nodules or lesions marked by at least 1 radiologist	7371

The main means of identifying the existence of cancer in the LIDC database is via diagnostic data. Selecting the ratings for the diagnostic data that the triplet CBMIR system was trained on was a crucial step in the procedure. Furthermore, the system's efficacy was assessed by comparing its results to the ratings provided by radiologists in the database. It is interesting to note that the database contains observations for lesions that range in size from three millimetres to thirty millimetres. These annotations are denoted by yellow boxes.

For all experiments, we used the complete LISS and LIDC-IDRI datasets after removing corrupted or incomplete scans. From the LISS dataset, 252 patients contributed 511 2D CISL images and 19 patients contributed 166 3D CT volumes (9 nodule categories). From the LIDC-IDRI dataset, 1,018 CT volumes from 1,010 patients were used, containing 7,371 nodules annotated by four radiologists. Benign and malignant labels for LIDC-IDRI were derived from the official diagnostic data (ratings: 1 = benign, 2–3 = malignant). For LISS, the lesion type annotations provided with the CISL dataset were mapped into benign and malignant classes based on radiological definitions.

For both datasets, we adopted a standardized pre-processing and splitting protocol. All CT slices were normalized to the range [0, 1], resized to 128×128 pixels for segmentation and classification, and separated into 80% training and 20% testing splits using 5-fold cross-validation. No patient overlap occurred between folds. This ensures consistent handling of both LISS and LIDC-IDRI datasets.

3.2. Image Pre-Processing

3.2.1. RGF Method

One of the most effective filters for rapidly converging and preserving edges is rolling guidance filtering (RGF). RGF has been widely used in various applications, including image fusion and augmentation. Goyal et al. [33] employed rolling guidance filtering and cross-bilateral filtering to propose a novel method for multi-modal image fusion. The fusion results from this process are both aesthetically pleasing and of high quality, as indicated by quantitative measurements. Prema et al. [34] introduced multi-scale, multi-layer rolling-guidance filtering, a sophisticated technique for combining visible and infrared data. This method divides images into three layers: base, macro, and micro. The proposed method utilizes several fusion techniques suitable for different scales. For micro-scale layers, it applies a phase-congruency-based fusion technique; for macro-scale layers, it uses an absolute maximum-based consistency verification fusion rule; and for base layers, it employs a weighted energy-related fusion strategy. Unlike many other modern fusion techniques, this method preserves crucial background and target information from the original images while minimizing the introduction of undesirable artifacts and unclear boundaries.

Chen et al. [35] described an image fusion method using rolling guidance filtering and the Laplacian pyramid in another study. Their technique separates source images into structural and detail components using the Laplacian pyramid model for structural parts and the sum-modified Laplacian model for detail portions. According to their evaluations, this method outperforms other fusion techniques. Additionally, Lin et al. [36] made a significant contribution to the field of image fusion by developing a novel technique for adaptively combining visible and infrared images. Their method preserves fine details and improves contrast in the fused image by combining saliency detection and rolling guidance filtering.

The filtered image U is defined as follows in equation (1) in this paper:

$$U = RGF(I, \sigma_s, \sigma_r, T) \quad (1)$$

where T represents the number of iterations, σ_s stands for standard deviation, and σ_r controls the spatial along with range weights, respectively.

3.2.2. *LFE Method*

LFE is particularly well-suited for handling nonlinear and complex medical images. In medical imaging, CT scans often contain regions with varying textures and densities that traditional image preprocessing techniques may struggle to capture effectively. LFE helps quantify the complexity and randomness in these local image regions, providing more detailed and rich feature representations. This additional level of detail is critical for improving segmentation and classification accuracy, especially when dealing with challenging cases such as early-stage lung cancer. Fractional entropy has been suggested by researchers as a useful tool for solving fractional nonlinear problems [37]. LFE, or Tsallis entropy, is a technique used to improve noise reduction.

The following fractal entropy coefficients in equation (2) as follows:

$$\begin{aligned}(U_\mu)_0 &= \frac{\mu^2}{(1-\mu)\Gamma(1+\mu)} h_0^{\mu-1},\\ (U_\mu)_1 &= \frac{\mu^2}{(1-\mu)\Gamma(1+\mu)} h_1^{\mu-1},\\ (U_\mu)_2 &= \frac{\mu^2}{(1-\mu)\Gamma(1+\mu)} h_2^{\mu-1}\end{aligned} \quad (2)$$

where $(U_\mu)_{\mathrm{m}} \in [0,1]$, $\mu \in [0,0.6]$ in the above equation.

After the preprocessing phase, the images are segmented using LW-convMLP UNet, which is described in detail below.

4. Methodology

4.1. Training Process

To improve the clarity of the experimental setup, we explicitly define the training environment, hyperparameter settings, optimization procedures, and evaluation metrics used throughout the study. All models—including baseline networks and the proposed LW-convMLP UNet + DRNet-MM classifier—were trained under identical conditions to ensure a fair comparison.

The model training was conducted on an NVIDIA T4 Tensor Core GPU using Python 3.6 and the PyTorch deep learning framework. The following steps were applied:

Data Splitting: The datasets, LIDC-IDRI and LISS, were divided into 80% training data and 20% testing data. We used a 5-fold cross-validation technique to ensure robust performance and mitigate overfitting.

Data Augmentation: To improve generalization and prevent overfitting, we applied data augmentation techniques, including random rotation, horizontal flipping, and scaling to the input CT images.

Hyperparameters:

- Learning Rate: 0.001, with a decay rate of 0.1 after every 10 epochs.
- Batch Size: 16 for training and 32 for testing.
- Number of Epochs: The model was trained for 50 epochs, with early stopping applied when validation loss stopped improving after 10 consecutive epochs.
- Optimizer: The Adam optimizer was used with default parameters (beta1 = 0.9, beta2 = 0.999), as it efficiently handles the stochastic gradient descent (SGD) updates, especially in deep learning models with high-dimensional inputs.
- Loss Function: A binary cross-entropy loss was used for the classification task and a Dice loss for the segmentation task, ensuring better performance on imbalanced classes.

Model Checkpoints and Regularization: Model checkpoints were saved at the best-performing epochs based on validation accuracy. Dropout layers were applied with a dropout rate of 0.5 to avoid overfitting during training.

Evaluation Metrics: The model was evaluated using standard metrics such as accuracy, precision, recall, F1-score, and AUC to ensure both segmentation and classification performance are adequately captured.

Training Time: The total training time for the model was approximately 8 hours for the LIDC-IDRI dataset and 4 hours for the LISS dataset.

All dataset partitions were created strictly at the patient level to prevent leakage across training, validation, and test sets. No CT slice, 2D patch, 3D volume, or augmented image originating from the same patient was allowed to appear in more than one partition. The 80–20 split was therefore performed at the patient ID level, followed by 5-fold cross-validation, also at the patient level. This ensures that the exceptionally high reported accuracies are not influenced by unintended overlap between training and testing samples.

4.2. LW-convMLP UNet Segmentation

The LW-convMLP UNet is a novel lightweight medical image segmentation network introduced to reduce the model's parameter count without compromising accuracy. The network comprises two crucial stages: the Conv stage and the MLP stage, integrating Convolutional Neural Networks (CNN) and Multi-Layer Perceptrons (MLP). Within the Conv stage, three Latent Discriminative Analysis (LDA) modules are employed to downsample the input, maintaining robust feature-extraction capabilities and reducing model complexity. Conversely, the MLP stage effectively integrates contextual information, facilitating deep tumor extraction through two layers of Latent Multi-Layer Perceptron (LMLP) modules. These modules enable the model to focus on local details and enhance feature representation by emphasizing high-level image information. The encoder's design adheres to these principles, while the decoder employs a symmetrical structure. The UNet design is applied throughout the entire model to ensure the incorporation of both low-level detailed features and high-level picture features. Furthermore, the model's performance is augmented by skip connections between the encoder and decoder components. Each module is explored in detail in the following section to provide a comprehensive understanding of the suggested method's benefits and functionality.

(A) LDA Module

A novel lightweight module named LDA-A has been developed to balance the accuracy (ACC) and complexity of lung tumor image segmentation models. This module incorporates two crucial stages to enhance its effectiveness.

The module utilizes depth-wise separable Convolution (Conv) to map feature channels and reduce computational load after initially capturing features using traditional Conv with downsampling. Moreover, it introduces non-linear features through Batch Normalization (BN) operations, improving model efficiency during training. Additionally, these operations enable the quick integration of feature map data through addition (ADD) operations. To further reduce computational complexity and redundancy, asymmetric Conv is employed instead of depth-wise separable Conv in the second stage. Several factors influence this decision. Firstly, asymmetric Conv proves to be more effective given the current lower channel count. The model performs better in various scenarios due to its increased flexibility in accommodating targets with different aspect ratios. Furthermore, the use of residual connections enables the development of a deep neural network with improved performance, addressing issues related to gradient vanishing and explosion. Through ADD operations, these residual connections facilitate the fusion of both shallow and deep information.

The LDA module employs the ADD operation for feature fusion, which is more efficient than the Concatenation operation. Concatenation necessitates complex memory copying on hardware, incurring significant computational costs. Although Concatenation is Flops-free and parameter-free, in practice, using ADD operations for feature fusion significantly reduces computational costs.

Here's another method of summarizing the computations inside the LDA-A phase using equations (3) through (10) for a clear illustration:

$$\mathrm{Y_{PO1}} = \mathrm{Conv_1}\ (\mathrm{X}) \tag{3}$$

$$\mathrm{Y_{PO2}} = \mathrm{DWConv}(\mathrm{Y_{PO1}}) \tag{4}$$

$$\mathrm{Y_{PO3}} = \mathrm{ADD}(\mathrm{Y_{PO2}}, \mathrm{BN}(\mathrm{Conv}\ (\mathrm{X}))) \tag{5}$$

$$\mathrm{Y_{PT1}} = \mathrm{Conv_1}\ (\mathrm{Y_{PO3}}) \tag{6}$$

$$\mathrm{Y_{PT2}} = \mathrm{ASConv_{1\times3}}\ (\mathrm{Y_{PT1}}) \tag{7}$$

$$\mathrm{Y_{PT3}} = \ \mathrm{ASConv}\ _{3\times1}(\mathrm{Y_{PT22}}) \tag{8}$$

$$\mathrm{Y_{PT4}} = \mathrm{ADD}\left(\mathrm{Y_{PT}}, \mathrm{BN}\big(\mathrm{Conv}(\mathrm{Y_{PO3}})\big)\right) \tag{9}$$

$$\mathrm{Y} = \mathrm{ADD}(\mathrm{Y_{PT4}}, \mathrm{X}) \tag{10}$$

This innovative design presents a brand-new element called LDA-B, represented by the variable X, which functions as a feature representation. X contains a number of component elements, including DWConv (depthwise Conv), Conv1 (1 × 1 kernel Conv), BN (batch normalization), and ASConv (asymmetric Conv) (Part I). The main aim of adding the LDA-B module is to improve the model's capacity to concentrate on particular areas of interest. This improvement is attained by highlighting important feature mappings while decreasing the impact on less important ones.

The final two Conv stage components are modified in this innovation. More specifically, as Figure 5 shows, a SE (Selective Excitation) module has been added to LDA after the first ADD operation. Based on global data, the SE module helps to suppress underperforming channels and selectively improve the performance of individual channels. This augmentation leads in improved model performance at a relatively small additional cost, despite somewhat increasing the number of model parameters and computational workload. It is crucial to stress that the addition of the SE module improves the model's generalization abilities in addition to sharpening its focus on the target region.

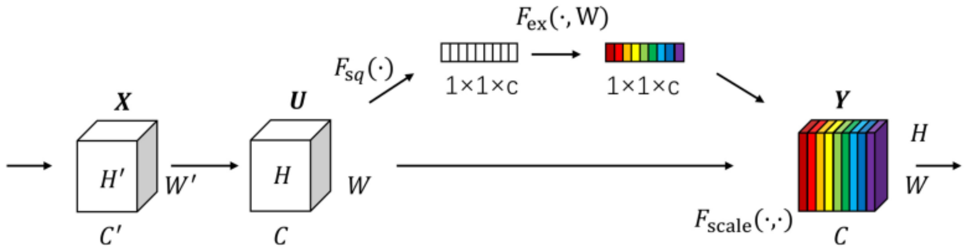

Figure 5. Detailed structure of SE module.

The two main functions of the SE module are "squeeze" and "excitation." Equation (11) defines the "excitation" function in terms of the "squeeze" operation's result. The SE module multiplies the result of the "excitation" function by the initial input features to get its final output:

$$Z = F_{sq}(f) = \frac{1}{H \times W} \sum_{i=1}^{H} \cdot \sum_{j=1}^{W} (i, j) \tag{11}$$

Z is a result of the squeeze process in the specific instance that is being described, where the function F_{sq} performs this operation. The variable "f" represents a set of two-dimensional feature maps, $f \in R^{H \times W}$, where each element in the set is represented by the variable $f(i, j)$. The feature map space's height and width are represented by the symbols H and W, respectively. The excitation operation is defined as follows in equation (12):

$$S = F_{ex}(Z, W) = \sigma\big(W_2 \delta(W_1 Z)\big) \tag{12}$$

Function F_{ex} in given context symbolically represents the excitation operation's result, indicated by "S.", and the Sigmoid and ReLU excitation functions are denoted by the symbols σ and δ ,respectively. Furthermore, W_1 and W_2 are individual components of a matrix of dimensions $W_1 \in R^{(C/r)} \times C$ and $W_2 \in R^{C \times (C/r)}$, respectively. The reduced dimensional coefficient is indicated by the value of r.

Following the excitation process, the original input features are multiplied by the output weights to have:

$$y = F_{scale}(f, S) = S \cdots f(i, j) \tag{13}$$

The final result of the SE module uses the symbol 'y' to stand for a particular value, $y = [y_1, y_2, \ldots, y_c]$; F_{scale} is the scale operation in equation (13).

It is appropriate to include equations (11) – (13) in order to represent the LDA-B equations.

(B) LMLP Module

Accurate results are difficult to achieve when dealing with image segmentation tasks because it is often difficult to distinguish the segmented region from the background. Modern methods seek to boost segmentation efficiency by incorporating ever more complex data. Nevertheless, the large number of parameters and high computational requirements of these methods often make them unsuitable for lightweight applications.

This study presents a novel LMLP module as a solution to this problem. This section uses shifting as a key component of a transformation process that modifies the original input image's attributes. The input image that was initially arranged in a 1-dimensional sequence is converted into a token series. The horizontal Multilayer Perceptron (MLP) operations are carried out using these tokens as their foundation. Furthermore, the module incorporates deep convolutional layers (DCL) to improve feature representation. This results in a decrease in the number of parameters required while also improving the retention of positional information and feature relationships. After additional vertical MLP operations, the tokens go through a DCL for better tumor extraction. The module effectively addresses the blurriness issue at the boundary between the background and lung tumor segmentation areas and effectively focuses on local details by performing MLP operations at a deep level in both horizontal and vertical directions on the relatively abstract and intricate input features.

To integrate more feature information, the LMLP module also includes two ADD operations. While the second ADD operation synchronizes the vertically acquired features—obtained prior to the MLP stage—with the features derived via DCL, the first ADD action combines the initial tokens with the properties of the DCL. The model becomes more flexible and resilient as a result of these numerous ADD operations, which also improve the module's expressive capacity. The output of the LMLP module goes through an extra-layer normalization process called LN. By removing any mean offset, this LN operation improves the training process's steadiness and guarantees that the outcome of the module is reliable. These insights are then utilized in the next phase in order to complete the lung tumor segmentation.

Moreover, the residual connection mechanism included in the LMLP module makes it easier to fuse feature maps with different dimensions. The module itself consists of two branches: one for segmentation tasks at high resolution and another for general image feature capture at lower resolutions. The LMLP module can handle complex image structures with ease thanks to its multi-branch structure. Equations (14) and (21) provide a summary of the calculations made within the LMLP block, as explained below.

$$\mathrm{X_T} = \mathrm{Shift\ (Tokenize\ (X))} \tag{14}$$

$$\mathrm{Y_{W1}} = \mathrm{MLP_W\ (X_T)} \tag{15}$$

$$\mathrm{Y_{W2}} = \mathrm{DWConv\ (Y_{W1})} \tag{16}$$

$$\mathrm{Y_{W3}} = \mathrm{ADD\ (Y_{W2} + X_T)} \tag{17}$$

$$\mathrm{Y_{H1}} = \mathrm{MLP_H\ (Y_{W3})} \tag{18}$$

$$\mathrm{Y_{H2}} = \mathrm{DWConv\ (Y_{H1})} \tag{19}$$

$$\mathrm{Y_{H3}} = \mathrm{ADD\ (Y_{W3} + Y_{H2})} \tag{20}$$

$$Y = X + Y_{H3} \tag{21}$$

W denotes a width-based operation, H denotes a height-based operation, and DWConv stands for depth Conv in this context. X stands for the input features.

The LMLP module, developed for solving image segmentation challenges, uses a multi-branch architecture to achieve its goal, strong spatial locality, and advantages in terms of computational and spatial efficiency.

4.2.1. LW-convMLP UNet Architecture

Table 2 gives a thorough overview of the lightweight encoder-decoder design that the LW-convMLP UNet uses [38]. The LDA-A module functions as the model's introductory component and is its fundamental component. The first part of this module focuses on reducing the dimensionality of the data by using traditional Conv techniques for tumour extraction. Then, depth-separable Conv methods are applied to effectively reduce feature channel changes, guaranteeing computational effectiveness. The second phase of the architecture expands the feature space by replacing depth-separable Conv with asymmetric Conv, which makes it possible for the model to effectively handle targets with several distinct aspect ratios. The LDA-B module smoothly moves to the second and third layers after the SE module is incorporated between the initial and next phases. This integration distinguishes the target area from the LDA-A module by enhancing the focus on it.

Table 2. Wide-ranging architecture of the LW-convMLP UNet proposed model.

Stage	Type	Layer	Channel (In)	Channel (Out)
Encoder	LDA-A	1	3	16
	LDA-B	2	16	32
	LDA-B	3	32	128
	LMLP	4	128	160
		5	160	256
		6	256	160
	Bilinear Up (x2)	7	160	160
	LMLP	8	160	128
	Bilinear Up (x2)	9	128	128

Decoder	LDA-B	10	128	32
	Bilinear Up (x2)	11	32	32
	LDA-B	12	32	16
	Bilinear Up (x2)	13	16	16
	LDA-A	14	16	3
	Bilinear Up (x2)	15	3	3
	SoftMax	16	3	1

The placement of each module is intentional:

- LDA-A → early encoder stage for robust low-level feature extraction.
- LDA-B with SE → mid-encoder stage to highlight clinically significant lung regions.
- LMLP → bottleneck stage for efficient global context modeling.
- Decoder blocks → reconstruct high-resolution masks using skip connections. This progression moves from local texture recognition to global tumor shape understanding in a parameter-efficient manner.

LMLP modules make up the fourth, fifth, and sixth layers of the architectural design. These modules operate in different orientations, which makes it easier to remove tumors completely. To lower the parameter count, a depth-separable Conv is added after each MLP module. This improves inter-feature correlations and positional awareness in the feature representation at the same time.

Computational costs were carefully taken into account to ensure the best possible computational efficiency. As a result, the model caps the number of channels at 256. This restriction strikes a balance between the model's performance and computational efficiency.

4.3. Classification using DRNet-MM Method

Using a novel technique, DRNet-MM applies masks to particular areas of image samples in an intentional manner. By using this technique, the original images are superimposed over these masked areas, enabling the model to produce more perceptive and comprehensible representations. There are three main parts to the DRNet-MM framework that are essential to its operation.

- **Autoencoder-classifier architecture**: This method starts with latent feature extraction from hidden images, which are then used to reconstruct the original images inside the hidden area. As a result, this process makes it easier to guess what the true labels for the hidden images are.
- **MM**: The procedure for determining the hidden region and constructing the objective function is described in this section. With the given input image samples, this information is essential for the autoencoder to effectively recover hidden image areas.
- **Training**: For tumor extraction, hidden images are fed into an autoencoder. It then reconstructs the hidden areas in the images during the forward pass and classifies the image according to the actual label. Using the calculated loss, the autoencoder-classifier's parameters are modified via backpropagation. Each element of the suggested method was introduced in the sections that followed.

TNM Staging and Multiclass to Binary Mapping:

The TNM staging system categorizes tumors (T), nodes (N), and metastases (M) into levels ranging from 0 to 4 (or X for M), forming numerous class combinations. To simplify this multiclass problem, TNM combinations were grouped into "benign" (e.g., T0M0N0) and "malignant" (e.g., T1M1N1) categories. This approach ensures clinical relevance by prioritizing early detection, where timely intervention is critical.

Data Imbalance Management:

To handle class imbalance, SMOTE oversampling was applied exclusively to the training subset, after the patient-level split was finalized. No synthetic sample generated by SMOTE was ever allowed to enter the validation or test sets. This prevents any artificial inflation of performance metrics. For both LISS and LIDC-IDRI, labels were assigned at the nodule level using validated diagnostic metadata, and slices were linked to their corresponding patient IDs to maintain class consistency across folds.

The mapping of TNM combinations to binary classification categories are presented in Table 3.

Table 3. Mapping of TNM Combinations to Binary Classification Categories

TNM Combination	Description	Binary Category
T0N0M0	No evidence of tumor, nodes, or metastasis	Benign
T1N0M0	Small localized tumor	Malignant

T2N1M0	Tumor with regional lymph node involvement	Malignant
T3N2M1	Advanced tumor with metastasis	Malignant
T4N3M0	Large invasive tumor without metastasis	Malignant
TxNxM0	Unknown tumor and node status, no metastasis	Benign
T1N0Mx	Small localized tumor, unknown metastasis	Malignant
T2N1Mx	Tumor with regional lymph nodes, unknown metastasis	Malignant
T0N0Mx	Normal tumor and nodes, unknown metastasis	Benign

4.3.1. *Autoencoder-Classifier Architecture*

Although the original DRNet-MM architecture supports complex-valued inputs for I/Q modalities, our implementation uses standard real-valued CT slices. All convolutional operations are purely real-valued, and the term 'complex' is retained only as historical naming from the original architecture. The masking strategy in this work operates on 2D image patches, not complex signal components. During training, a fixed proportion of patches is randomly hidden and the autoencoder learns to reconstruct them using contextual information from the visible patches. Figure 6 provides a visual representation of this idea to aid in comprehension.

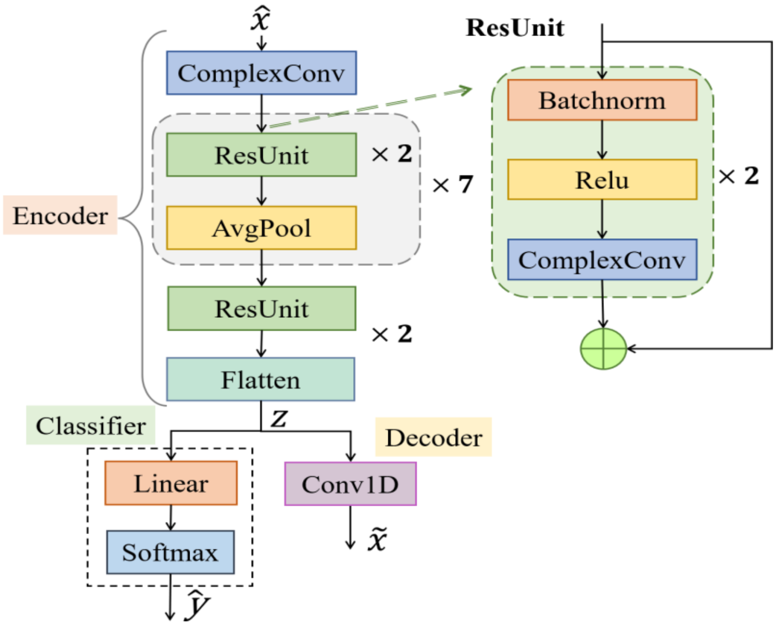

Figure 6. The autoencoder-classifier architecture's structure in CResNet.

Real residual neural network (R-ResNet) and C-ResNet's architectural layouts are fairly similar, except for the Conv layers, where C-ResNet applies a more complex Conv operation on the input picture. The real and imaginary components are combined by the Conv kernel of the complex Conv operation, as opposed to the real Conv operation, maintaining the feature connection and improving recognizing ACC in the process. Specifically, the input picture may be expressed as equation (22).

$$x = \begin{Bmatrix} I \\ Q \end{Bmatrix} = \begin{Bmatrix} \text{real }(x) \\ \text{imag }(x) \end{Bmatrix} \tag{22}$$

The Conv kernel of the neural network is $W = A + iB$, and the complex Conv operation is shown in equation (23) as,

$$F = (A^{*}I - B^{*}Q) + i(B^{*}I + A^{*}Q) \tag{23}$$

Moreover, feature dimensions increase in tandem with the depth of neural networks. In order to effectively compress features, this study adds a pooling layer after each Conv layer. The neural network also uses batch normalization, which accelerates convergence and boosts training effectiveness. Within the decoder of the system design shown in Figure 7, there is a Conv in one dimension having a kernel dimension of one. In order to obtain image features z, the classifier also includes the linear level, which in turn produces the projected class distribution, represented by ' $\grave{y}$.'

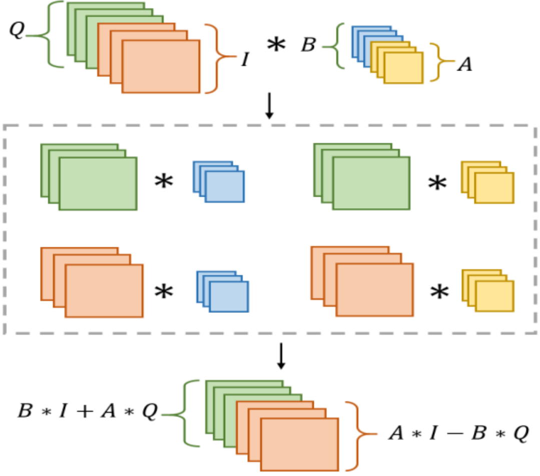

Figure 7. A good illustration of the sophisticated Conv operator.

4.3.2. *Masked Modelling*

The idea of MM is shown in Figure 8, with further information provided in references [39, 40]. This method uses two separate masks, called mask 1 and mask 2. Mask 1 is in charge of selecting 50% of the sample points at random from a given image, indicated by the letter "x," in the current study. Equation (24), when expressed mathematically, describes this process,

$$\grave{x} = x \odot M \tag{24}$$

The sequence M in the scenario is represented as $M = \{z(n) \mid n = 0,2,\cdots,K-1\}$, and it consists of binary values, that is, ones and zeros. The input signal, $\grave{x}$, is fed into an encoder during the encoding process. An output, x″, is then produced by using a lightweight decoder. Then, an additional mask, called "mask 2," is applied to the decoded image $\grave{x}$ as well as the original image x. The purpose of this mask is to cover the areas that "mask 1," the first masking operation, left exposed. The mathematical representation of these operations can be found in equations (25) and (26), which are explained below.

$$x' = x \odot (1 - M) \tag{25}$$

$$\grave{x}' = \grave{x} \odot (1 - \mathrm{M}) \tag{26}$$

In the given context, 'x'' indicates the demasked original lung tumor images, and '$\grave{x}'$' indicates the reconstructed images following the demasking procedure. The autoencoder's ability in reconstructing hidden portions of images from the visible elements is improved by the introduction of a novel loss function called the mean square error (MSE). Equation (27) is the expression for this loss function.

$$L_{MSE} = \frac{1}{N}\sum_{i=1}^{N} (x' - \grave{x}')^2 \tag{27}$$

The variable 'i' takes values between 1 and N $i = 1,2,\cdots,N$, where N is the number of image sample points found within the masked region of the given image.

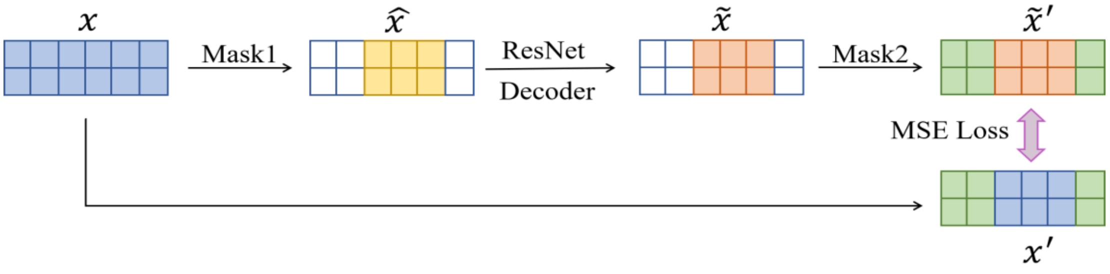

Figure 8. MM structure.

The masked modeling (MM) strategy is adapted for real-valued CT images by masking spatial patches, not complex components. The model learns to reconstruct hidden lung regions, encouraging stronger latent features that support downstream classification.

4.3.3. *Training Process*

In equations (28) and (29) during the training phase, the goal function L may be expressed as

$$\mathcal{L} = \mathcal{L}_{\mathrm{MSE}} + \mathcal{L}_{\mathrm{CE}} \tag{28}$$

$$\mathcal{L}_{\mathrm{CE}} = -y\log\, p_y \tag{29}$$

When it comes to image classification, "p_y" denotes the expected probability distribution across classes, and "y" denotes the actual label given to a particular image. "$\mathcal{L}_{\mathrm{CE}}$" Represents the loss of cross-entropy. In order to maximize the model's performance, the encoder, decoder, and classifier parameters are updated in a backward propagation step using the computed objective function for a mini-batch.

The classifier, decoder, and encoder weights are saved following the forward and backward propagation processes. The testing images are fed into the neural network during the testing procedure so that it can be classified. To achieve impressive ACC for the classification for lung tumor images, hyperparameter tuning is done after the classification process through the use of a brand-new, IGJO algorithm to optimize the DRNet-MM classifier.

4.4. U-Net Model Classification Process

The U-Net model, widely recognized for its performance in medical image segmentation, was adapted to perform classification tasks in this study. For consistency with other models, we made the following adjustments:

Data Preprocessing: The same preprocessing steps used for the proposed model were applied, including rolling guidance filtering (RGF) and local fractional entropy (LFE) for noise reduction on the LISS and LIDC-IDRI datasets. The images were resized to 128 × 128 pixels to maintain consistency with the input sizes used for other models.

Segmentation-Based Features: U-Net was primarily used to segment lung nodules from the CT images. From the segmented output, features such as tumor size, shape, and texture were extracted and passed to a classifier for final classification (benign vs. malignant).

Feature Extraction and Classification: A fully connected layer was added after the U-Net segmentation output to perform classification. The extracted features were fed into a softmax classifier to predict whether the detected tumor was benign or malignant. Cross-entropy loss was used for the classification task, and the model was trained with a learning rate of 0.001 using the Adam optimizer.

Evaluation: We used the same evaluation metrics (accuracy, precision, recall, F1-score, AUC) as used for the proposed model to ensure consistent comparison.

4.5. Hyperparameter tuning using IGJO

A. GJO Algorithm

Golden jackal hunting tactics serve as an inspiration for GJO, which is built on the swarm intelligence principles seen in nature. Three stages comprise the hunt: (a) locate the prey, (b) encircle and agitate, and (c) launch an attack on the prey [41]. In this study, IGJO was applied specifically to optimize four critical hyperparameters of the DRNet-MM classifier: learning rate, dropout rate, batch size, and masking ratio. The objective was to maximize the validation F1-score during patient-level 5-fold cross-validation. IGJO improved F1 by 1.4% on LIDC-IDRI and 2.1% on LISS compared with manual tuning. All baseline models (UNet, ResNet, GoogleNet, ShuffleNet) were also tuned using grid or random search within comparable ranges to ensure a fair comparison. The GJO algorithm's mathematical model is developed in the following.

(i) Search Model

First, the prey is dispersed over a matrix that is generated at random. In this matrix, the symbols 'N' and 'n' stand for the presence of prey populations and spatial dimensions, respectively.

(ii) Exploration Stage

Jackals are adept at following their prey, which makes it difficult to catch them. As such, these jackals wait patiently for their chance to attack another possible prey. We used the equations (30) and (31) to describe their hunting behavior when ($|E| > 1$):.

$$Y_1(t) = Y_M(t) - E \cdot |Y_M(t) - rl \cdot \mathrm{Prey}(t)| \tag{30}$$

$$Y_2(t) = Y_{FM}(t) - E \cdot |Y_{FM}(t) - rl \cdot \mathrm{Prey}\ (t)| \tag{31}$$

The hunting position is indicated by the algorithm through the use of a vector labeled "prey (t)". It's crucial to remember that this iteration is still in progress. Moreover, the algorithm keeps track of the positions of the male and female jackals, identified as "$Y_M(t)$ and $Y_{FM}(t)$ " respectively, continuously. The labels "$Y_1(t)$ and$Y_2(t)$" indicate these jackals' most recent locations. The following formulas are used to determine the prey's escape energy(E): equations (32) and (33) as,

$$E = E_1 \cdot E_0,\ E_0 = 2 \cdot r - 1 \tag{32}$$

$$E_1 = c_1 \cdot \left(1 - \frac{t}{T}\right) \tag{33}$$

Here, E_0 represents a value that was generated at random between -1 and 1. The variable T represents the upper bound on the number of iterations that are permitted, and the constant cc_1 has a fixed value of 1.5. The descending energy of the prey is indicated by E_1.

The relationship between the jackal and its prey is quantified by the expression$|Y_M(t) - rl \cdot \text{Prey }(t)|$. In this case, "rl" stands for a vector made up of random numbers obtained from the equations (34) and (35), which describe the Le'vy flight function (LF).

$$rl = \frac{5 \cdot LF(y)}{100} \tag{34}$$

$$LF(y) = \frac{\mu \cdot \sigma}{100 \cdot \left| v^{\left(\frac{1}{\beta}\right)} \right|},\ \sigma = \left\{ \frac{\Gamma(1+\beta) \cdot \sin\left(\frac{\pi\beta}{2}\right)}{\Gamma\left(\frac{1+\beta}{2}\right) \cdot \beta \cdot \left(2^{\beta-1}\right)} \right\}^{\frac{1}{\beta}} \tag{35}$$

Here, the variable v stands for values chosen at random from the open interval (0, 1), while the symbol β stands for a constant with a fixed value of 1.5.

$$Y(t+1) = \frac{Y_1(t) + Y_2(t)}{2} \tag{36}$$

The updated position of the prey with respect to the jackals is represented by the symbol $Y(t+1)$ in equation (36).

(iii) Exploitation (Besieging and Swallowing Prey)

Studies have demonstrated that the existence of golden jackals may hinder their prey's ability to flee. A mathematical model is provided by equations (37) and (38) to explain how jackals behave when they are pursuing and eating prey, particularly in situations where the absolute value of 'E' is equal to or less than $1(|E| \leq 1)$.

$$Y_1(t) = Y_M(t) - E \cdot |rl \cdot Y_M(t) - \text{Prey }(t)| \tag{37}$$

$$Y_2(t) = Y_{FM}(t) - E \cdot |rl \cdot Y_{FM}(t) - \text{Prey }(t)| \tag{38}$$

(iv) Phase of Exploration to Exploitation and Convergence Transition

It makes it easier for the GJO algorithm to move from an early exploration stage to a phase where the system successfully uses its prey's unstable energy resources. The prey's energy level drops dramatically when it tries to escape. The study was made to develop a model for the prey's escape energy to take this into consideration. At the beginning of each iteration, the prey's energy, represented as $|E|$, is randomly perturbed between -1 and 1. A drop throughout 0 to -1 indicates that the prey is under immediate risk, and a rise of 0 to 1 indicates the prey's abilities have improved. The prey faces increasingly difficult obstacles in its fight for survival with every iteration that follows. Pairs of jackals hunting begin exploring different areas of the search space when the value of E rises above 1. On the other hand, the emphasis moves to the exploitation stage, where the prey is actively sought after, when the absolute value of E drops below 1.

The first step of the GJO algorithm looks at a population of pre-selected solutions. A pair of jackals makes an estimation of the prey's location as the algorithm develops. Every potential solution modifies its location in relation to the pair of jackals. Through a step-by-step reduction of $|E| < 1$, the algorithm efficiently manages both the discovery and mining stages. When E is greater than 1, the jackal pair approaches the prey in preparation for an attack; when E is less than 1, they retreat from the prey to investigate. The GJO algorithm ultimately ends when a set of convergence criteria are satisfied. Algorithm 1 contains the GJO pseudo-code for reference, and Table 4 offers more information about the GJO algorithm.

Table 4. GJO algorithm

Algorithm 1. An illustration of the pseudo-code of the GJO

```
Inputs: Consider the variables T, which stands for the maximum number of iterations, and N, which stands for the size of the population.
Outputs: The prey's location and degree of survival suitability.
Define $Yi$ as the initial population of prey, where i is a random variable between 1 and N that represents the total number of prey $Yi(i = 1,2, \dots, N)$.
While ( $t < T$ )
Find out the fitness scores of the prey.
```

```
$Y_1 =$ "the best target species (the location of the male jackal)"
$Y_2 =$ second best prey individual (location of the female jackal)
for (each of the preys)
Update the escaping energy " $E$ "
Update " $rl$ "
If ( $|E| \leq 1$) (Exploration phase)
Adjust the target position.
If ( $|E| > 1$) (Exploitation phase)
Adjust the target position.
end for
$t = t + 1$
end while
return $Y_1$
```

B. Overview of Improved GJO (IGJO)

Both premature convergence and the unequal distribution of exploration and exploitation present problems for the traditional GJO algorithm. To solve these problems and enhance the conventional GJO algorithm's performance, this study applies the direct rotational (RDR) technique that was first presented by Abualigah [42]. The current stage of the study has been completed with success thanks to this methodology. In order to assess the overall impact of finished stages, a thorough examination of all necessary elements is carried out [42]. The study uses equation (39) as described below to make the orthonormal basis.

$$x^{k+1} - x^{k+} = \sum_{i=1}^{n} \lambda_i \cdot d_i \quad (39)$$

The guidelines are as follows: The number of variables that have produced successful results is represented by λ_i, and the point that indicates the best search direction is indicated by $x^{k+1} - x^{k+}$. This leads to the placement of this point in the modified search path in equation (40).

$$pi = \begin{cases} d_{i,} & \lambda_i = 0 \\ \sum_{j=0}^{n} \lambda_j \cdot d_j & \lambda_i \neq 0 \end{cases} \quad (40)$$

Subsequently, equation (41) updates the search results derived from the Gram-Schmidt normalization procedure as follows.

$$qi = \begin{cases} p_i & i = 1 \\ p_i - \sum_{j=1}^{i-1} \frac{q_j^T \cdot p_i}{q_i^T \cdot q_j} & i \geq 2 \end{cases} \quad (41)$$

The modified and standardized search directives are defined by equation (42) as shown below.

$$d_i = \frac{q_i}{\|q_i\|}, i = 1,2,3, \dots, n \quad (42)$$

This method modifies the local search and then pursues the search in the opposite direction until the convergence criteria of the algorithm are met.

The complete configuration of each model, including architectural parameters, loss functions, optimizer settings, and IGJO-based hyperparameter tuning strategy, is documented to support reproducibility. The pseudocode for IGJO and the detailed pipeline from preprocessing to final classification are included to guide implementation.

5. Results and Discussion

The NVIDIA T4 Tensor Core GPUs, with 12.68 gigabytes of RAM and 78.19 gigabytes of storage, provide powerful computational power for the proposed deep learning (DL) model. These GPUs ensure smooth performance on Nvidia hardware when used with Python 3.6, enhancing the overall machine learning workflow with PyCharm 1.4.0. They prove particularly beneficial in the Google Colab setting, where they excel in tasks such as image classification and evaluating lung tumor detection efficacy. The utilization of crucial libraries, including CUDA, cuDNN, OpenCV, and others, enables the successful completion of these tasks.

5.1. Evaluation Metrics

In this study, standard evaluation measures were used; the measures used in this study were PR, F1, SP, DSC, JSC, FPR, AUC and ACC.

ACC in equation (43) measures the model's ACC and is expressed as the proportion of correctly identified images to all test images.

$$Accuracy\ (ACC) = \frac{TP+TN}{TP+TN+FP+FN} \quad (43)$$

F1 measures how many images were correctly identified out of all the testing images and assesses how accurate a model is expressed in equation (44).

$$F1-score\ (F1) = \frac{2*Precision*Recall}{Precision+Recall} \quad (44)$$

The percentage of accurate negative predictions compared to all actual negatives is referred to as SP in classification by equation (45).

$$Specificity\ (SPEC) = \frac{TN}{TN+FP} \quad (45)$$

AUC is a metric used to evaluate a model's capacity to distinguish between various outcomes. This metric is contained in the interval [0, 1].

The percentage of negative occurrences (or samples) that are mistakenly identified as positive is measured by the FPR. The following formula is used to determine the False Positive Rate in equation (46):

$$FPR = \frac{FP}{FP+TP} \quad (46)$$

The overlap between two sets is calculated using the DSC in equation (47), which divides the sum of the sizes of the two sets' sizes by the size of their intersection.

$$(DSC = (2*TP)/(2.TP+FP+FN)) \quad (47)$$

By calculating the intersection's size divided by its union, the JSC in equation (48) calculates the similarity between two sets.

$$JSC = TP/(TP+FP+FN) \quad (48)$$

5.2. Segmentation Analysis

Table 5. Segmentation Analysis of Datasets

Datasets	**Test ACC (%)**	**Test Loss (%)**	**DSC (%)**	**JSC (%)**	**Area Error (mm²)**	**AUC (*p*-Value)**
LISS	96.35	0.15	94.88	90.38	1.48	0.99 ($p < 0.001$)
LIDC-IDRI	96.10	0.17	92.35	86.07	2.63	0.98 ($p < 0.001$)

From Table 5 and Figure 9-11, segmentation analysis of LISS datasets shows that the test ACC achieved is 96.35%, the test loss is 0.15%, the DSC is 94.88%, the JSC is 90.38, the area error is 1.48 mm², and the AUC (p-value) is 0.99 (p<0.001). Segmentation analysis of the LIDC-IDRI dataset shows that Test ACC achieved is 96.10%, Test Loss is 0.17%, DSC is 92.35%, JSC is 86.07%, Area Error is 2.63%, and AUC (p-value) is 0.98 (p<0.001).

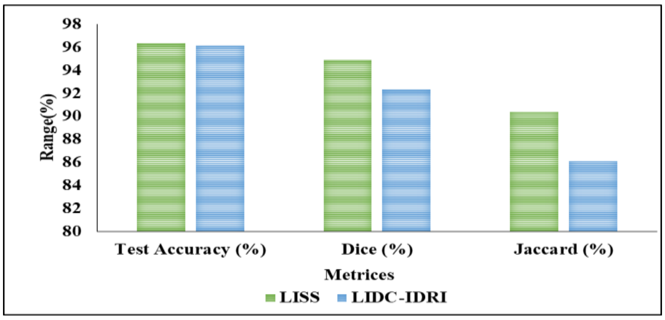

Figure 9. Segmentation analysis of Test ACC, DSC and JSC with LISS and LIDC-IDRI datasets.

5.3. Classification analysis of LISS and LIDC-IDRI datasets

The results illustrated in Figures 12-16 demonstrate the superior performance of the proposed model compared to existing models. Specifically, the proposed method achieves high accuracy, precision, and F1-scores for both the LISS and LIDC-IDRI datasets, outperforming traditional models such as GoogleNet, ShuffleNet, and ResNet. These results suggest that the integration of lightweight components, such as the LW-convMLP UNet and DRNet-MM, enhances the model’s ability to accurately segment and classify lung cancer images while maintaining efficiency.

The precision and AUC values achieved by the proposed model (90.25% precision, AUC of 0.96 for LISS, and 99.10% precision, AUC of 1.00 for LIDC-IDRI) are particularly notable, as they highlight the model's ability to handle the imbalance in medical datasets effectively. Furthermore, the proposed method's false positive rate (FPR) remains lower than that of existing models, which is critical in reducing unnecessary diagnoses or interventions in medical settings.

These results demonstrate the practical utility of the proposed method in medical imaging and highlight its potential for clinical application, where precision and reliability are paramount.

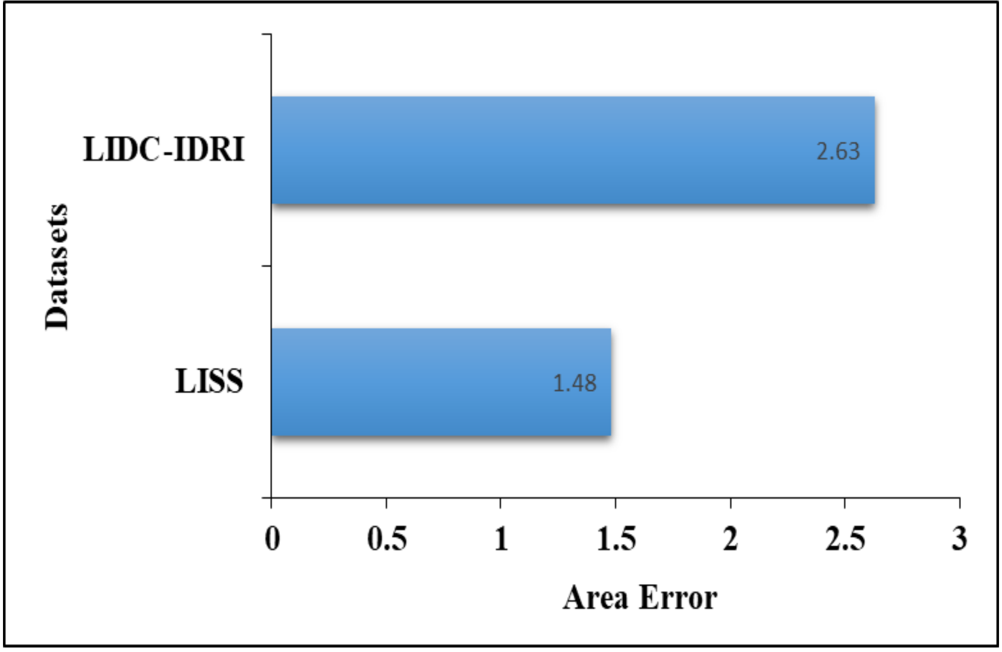

Figure 10. Area error analysis with LISS and LIDC-IDRI datasets.

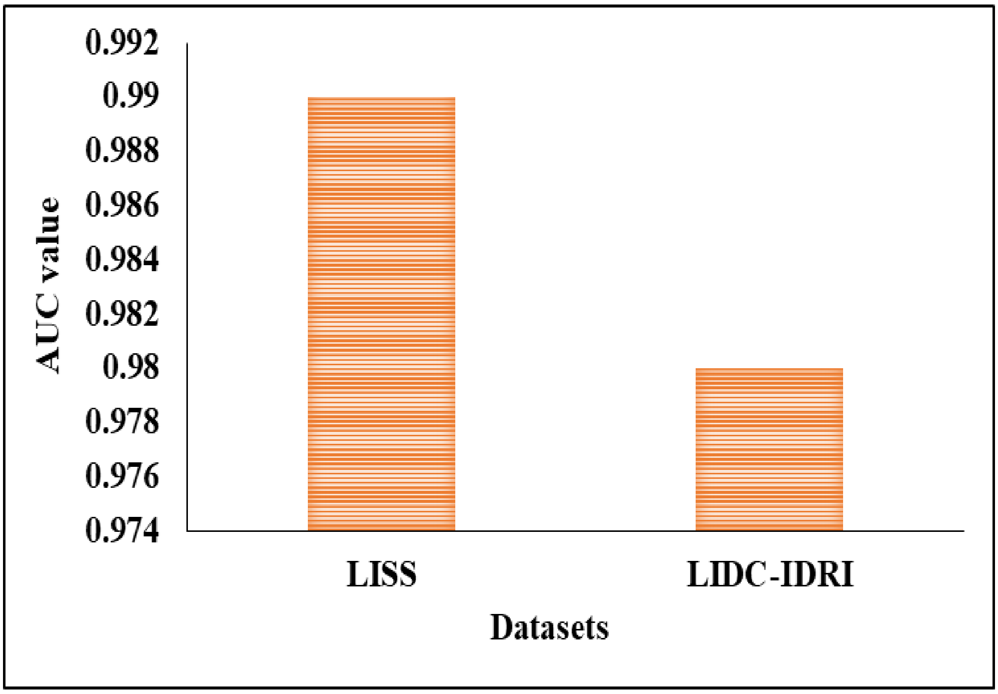

Figure 11. AUC value analysis with LISS and LIDC-IDRI datasets.

The results presented in Figures 17–21 clearly demonstrate the significant improvements the proposed model achieves compared to existing methods, particularly in terms of accuracy, precision, sensitivity, and false positive rate (FPR). The proposed model shows an exceptional accuracy of 99.4% and precision of 99.10%, making it one of the most reliable models for lung cancer detection. These metrics are critical in clinical settings, as they represent the model's ability to correctly diagnose malignant and benign tumors. Achieving such a high precision rate means the model is less likely to generate false positives, which is a significant concern in lung cancer screening where false alarms can lead to unnecessary biopsies or treatments.

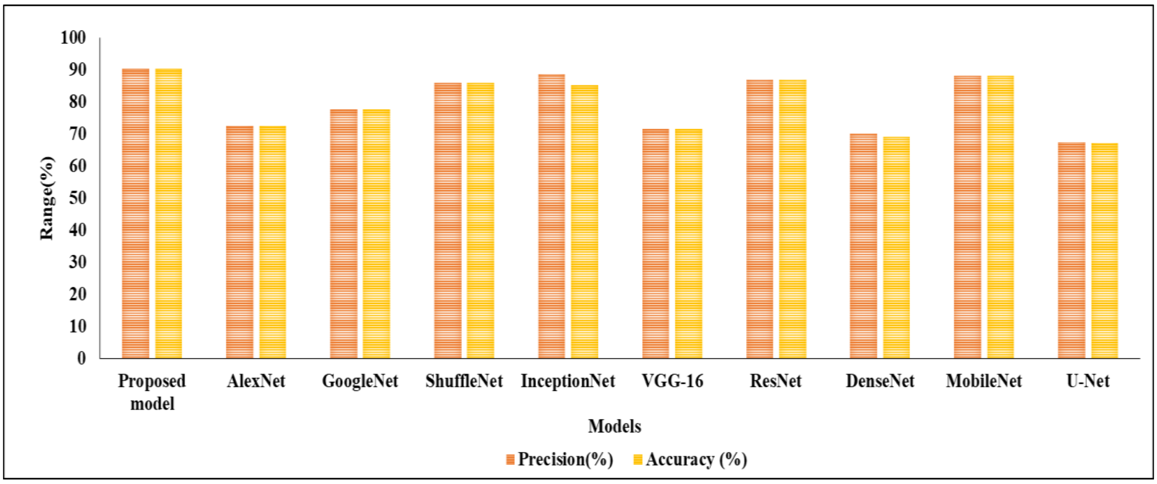

Figure 12. PR and ACC analysis of existing and proposed model of LISS dataset.

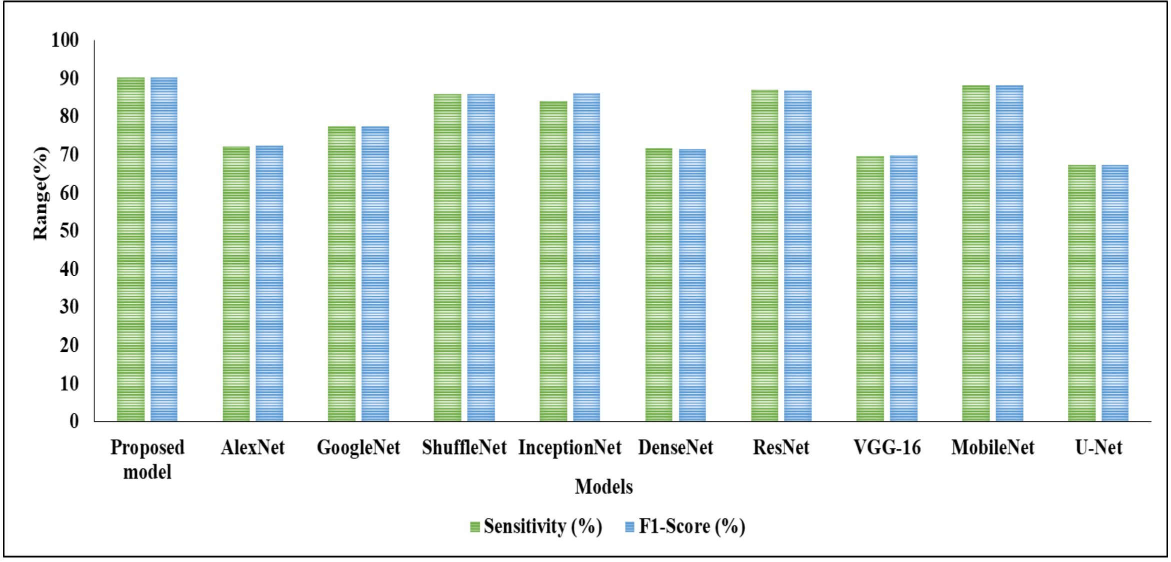

Figure 13. SEN and F1 analysis of existing and proposed model of LISS dataset.

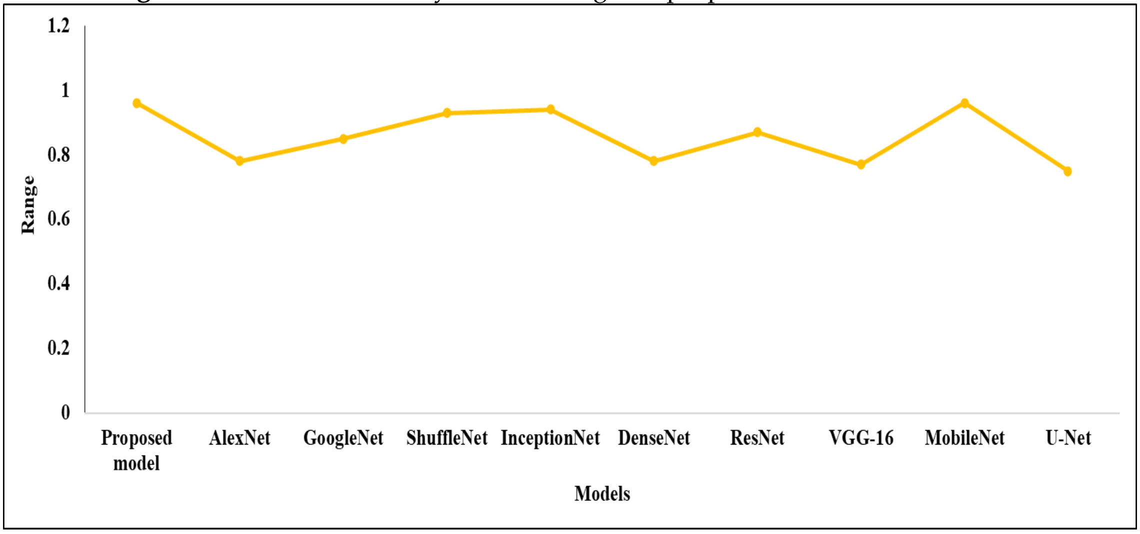

Figure 14. AUC analysis of existing and proposed model of LISS dataset.

Moreover, the model's sensitivity of 98.73% underscores its ability to accurately detect true positives, which is crucial for early-stage cancer detection. Early and accurate detection of malignant tumors can significantly improve patient outcomes by ensuring timely treatment. The model's high sensitivity, coupled with its precision, ensures a balance between detecting actual cancer cases while minimizing misdiagnosis. The low FPR of 0.003 further highlights the model's robustness in distinguishing between cancerous and non-cancerous lesions. False positives in medical diagnoses can result in costly and potentially harmful follow-up procedures. By maintaining a low FPR, the proposed model not only ensures higher diagnostic accuracy but also contributes to patient safety and reduces healthcare costs.

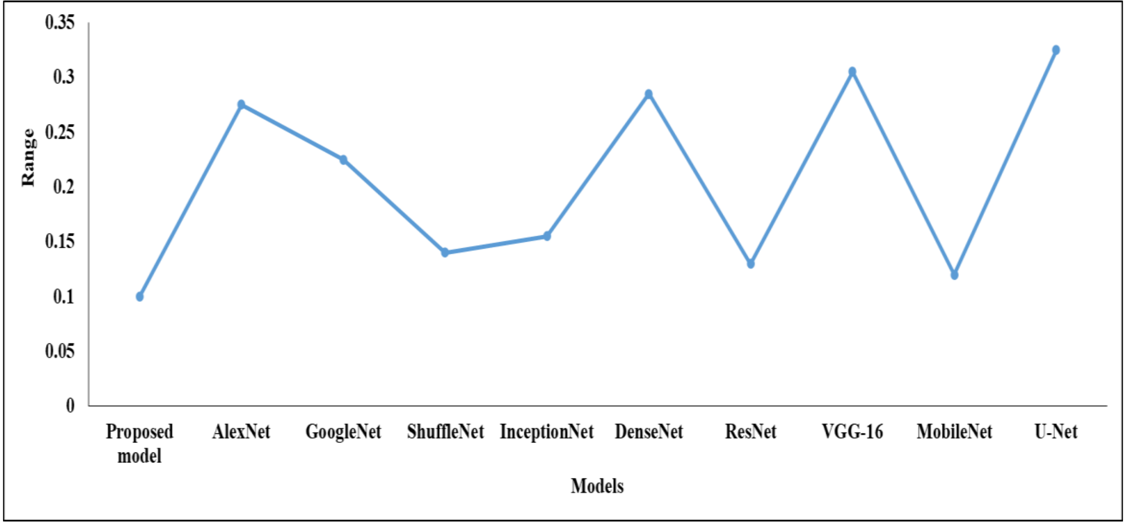

Figure 15. FPR analysis of existing and proposed model of LISS dataset.

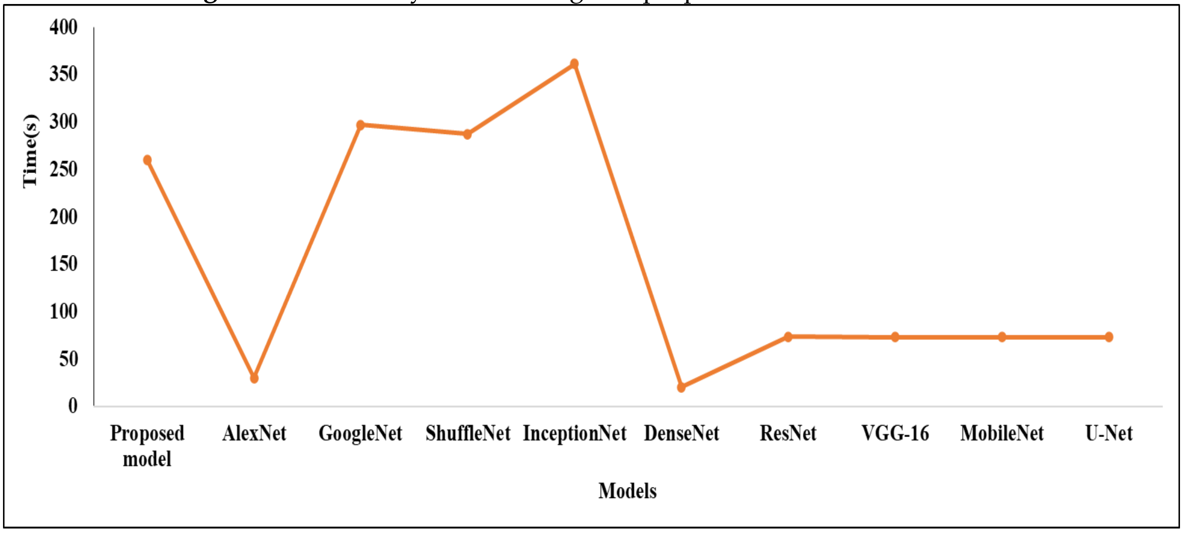

Figure 16. Time analysis of existing and proposed model of LISS dataset.

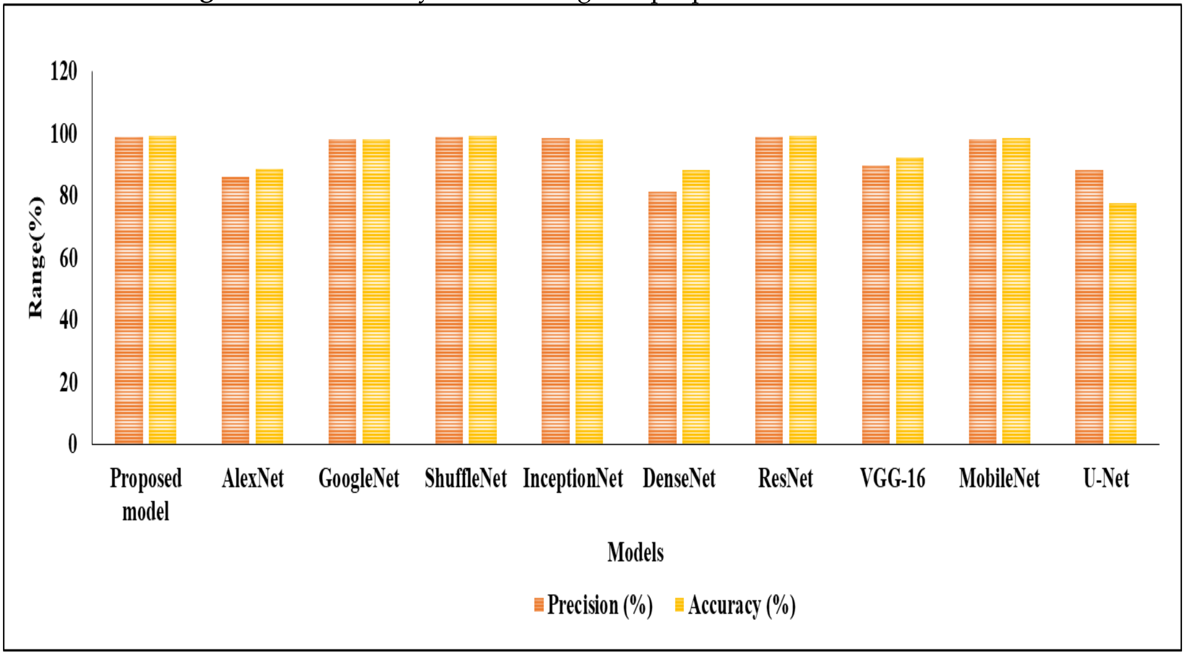

Figure 17. PR and ACC analysis of existing and proposed model of LIDC-IDRI dataset.

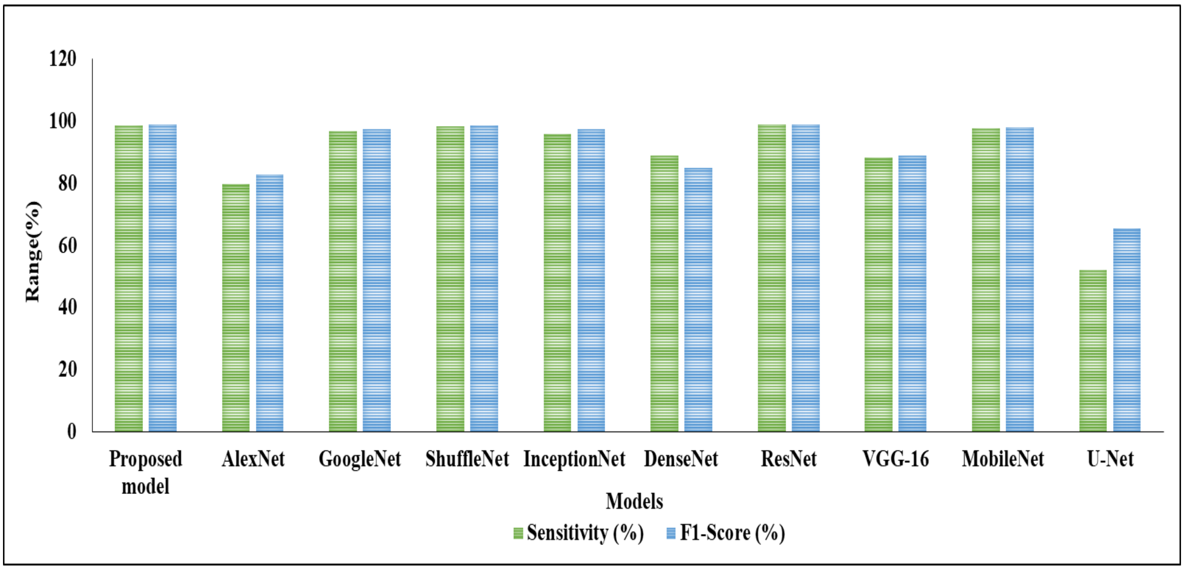

Figure 18. SEN and F1 analysis of existing and proposed model of LIDC-IDRI dataset.

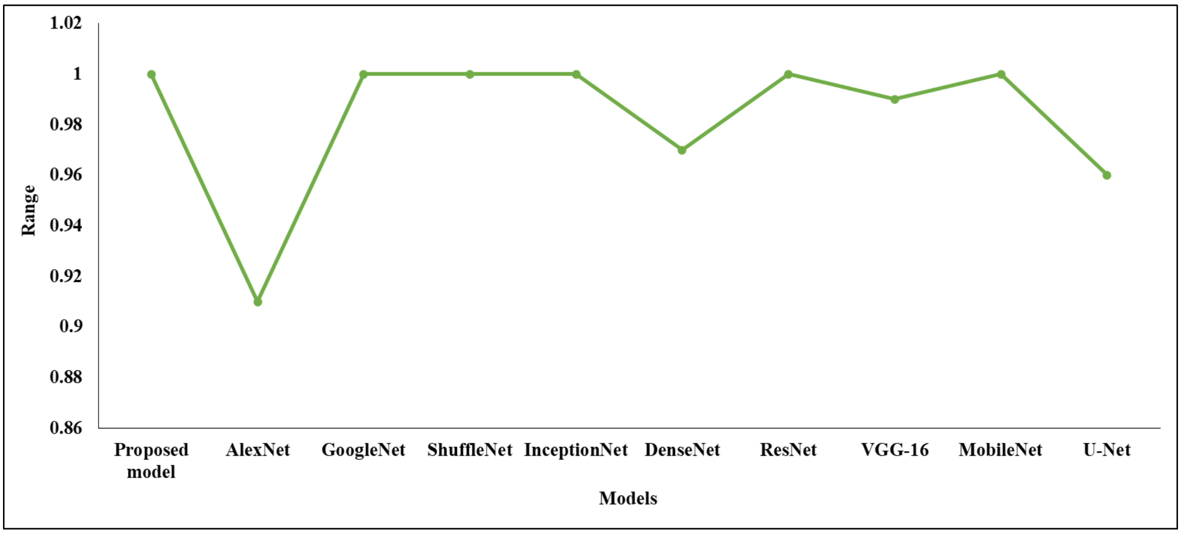

Figure 19. AUC analysis of existing and proposed model of LIDC-IDRI dataset.

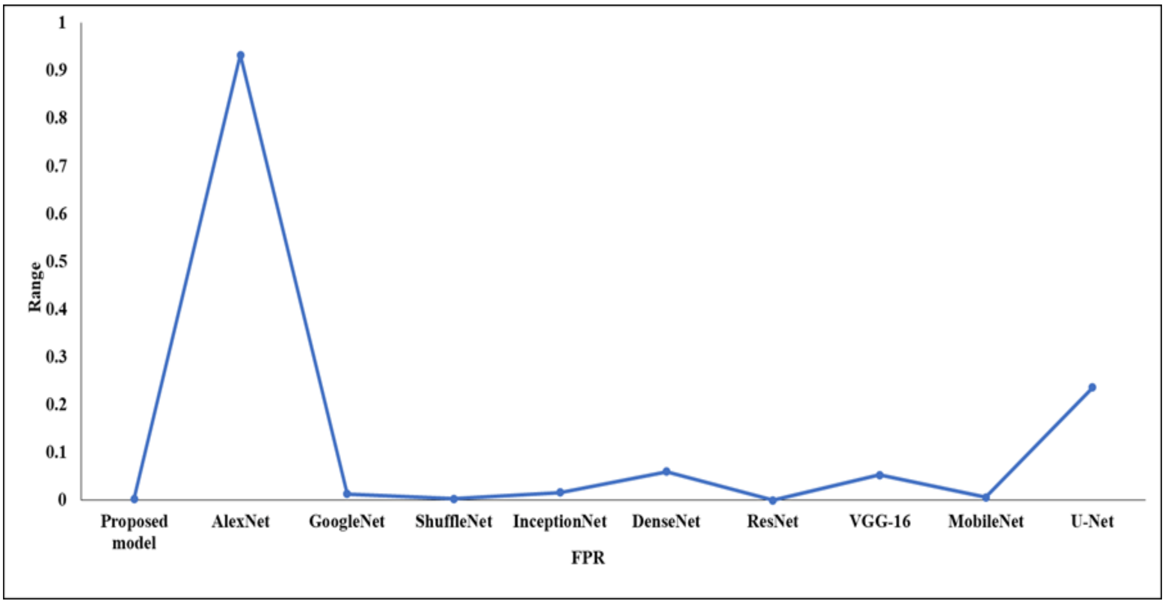

Figure 20. FPR analysis of existing and proposed model of LIDC-IDRI dataset.

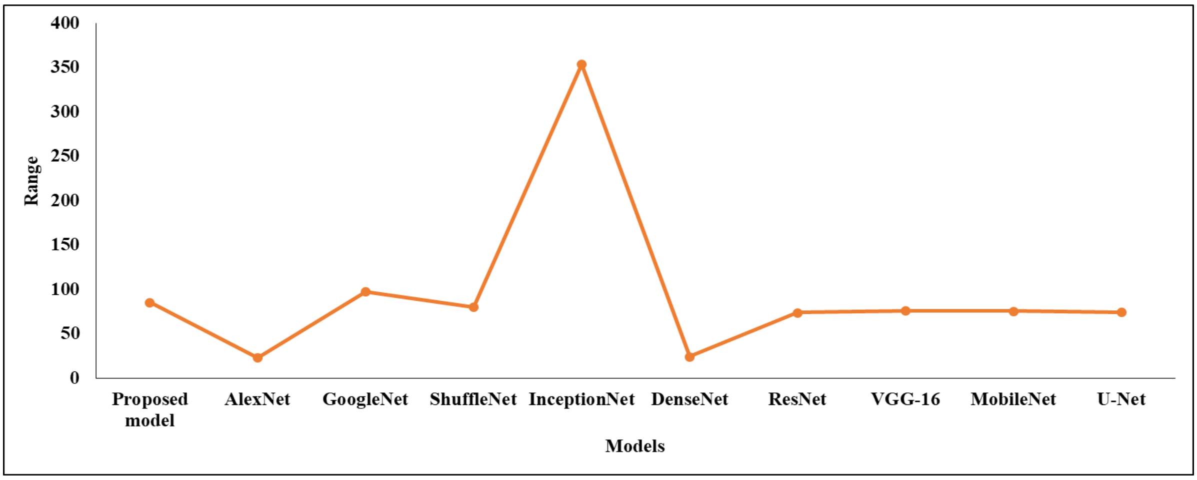

Figure 21. Time analysis of existing and proposed model of LIDC-IDRI dataset.

Table 6. ACC, PR, SEN and SP of Proposed classification method on two different sizes of input images: 64 × 64 and 128 × 128.

Datasets	Size of Input Images	ACC	PR	SEN	SP
LISS	128 × 128	90.29	90.29	90.29	96.76
	64 × 64	94.95	94.17	94.17	98.05
LIDC-IDRI	128 × 128	98.75	97.5	97.5	99.16
	64 × 64	98.62	**97.85**	**97.85**	**99.28**

From Table 6 and Figures 22 and 23, the dataset of LISS with a size of input images of 128 × 128 has achieved an ACC of 90.29%, a PR of 90.29%, a SEN of 90.29%, and a SP of 96.76%. The dataset of LISS with a size of input images of 64 × 64 had achieved an ACC of 94.95%, a PR of 94.17%, a SEN of 94.17, and a SP of 98.05%. The dataset of LIDC-IDRI with a size of input images of 128 × 128 had an ACC of 98.75%, a PR of 97.5%, a SEN of 97.5%, and a SP of 99.16%. The dataset of LIDC-IDRI with a size of input images of 64 × 64 had an ACC of 98.62%, a PR of 98.85%, a SEN of 97.85%, and a SP of 99.28%. The aim of Table 6 is to evaluate the impact of input image size on the classification performance of the proposed model. Specifically, we compare the model's performance when using two different input image resolutions (64 × 64 and 128 × 128) to determine how image size affects key metrics like accuracy, precision, sensitivity, and specificity.

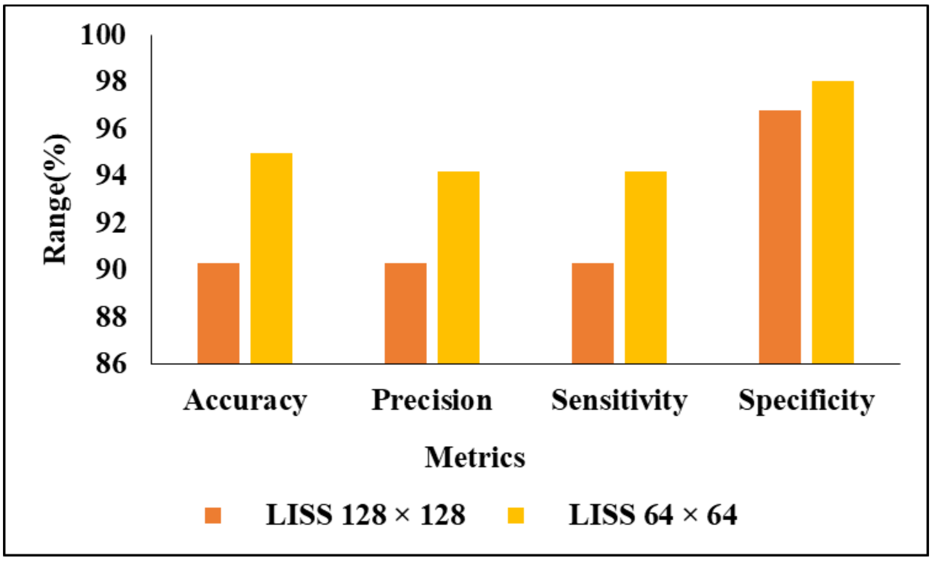

Figure 22. Proposed classification method for LISS dataset on two different sizes of input images.

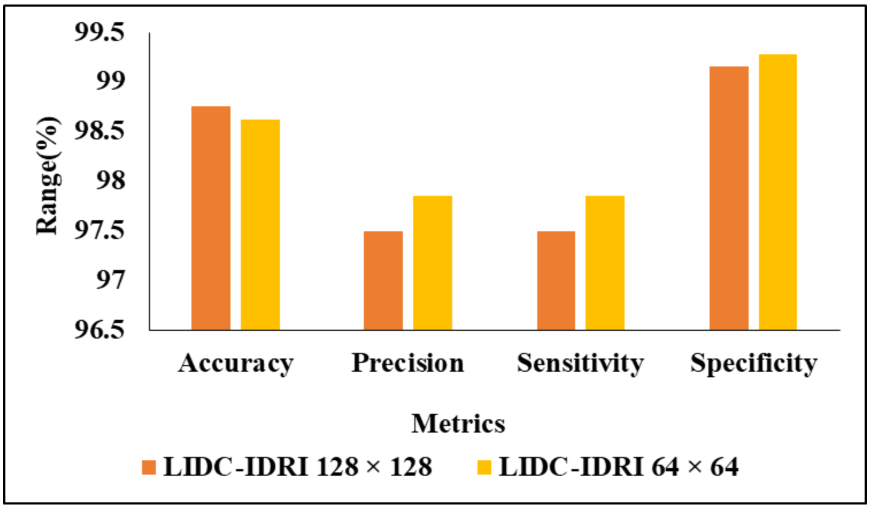

Figure 23. Proposed classification method for LIDC-IDRI dataset on two different sizes of input images.

The observed performance difference between the LIDC-IDRI dataset (99.4%) and the LISS dataset (90.25%) is primarily due to variations in data quality and consistency. LIDC-IDRI is a well-curated dataset with high-resolution CT scans and comprehensive annotations, which allows the proposed model to fully leverage its features. In contrast, LISS contains images of varying resolution and quality, with more subtle or ambiguous cases that are harder to classify. This suggests that the model is sensitive to differences in dataset quality, which affects its ability to generalize across different data sources. Despite the drop in accuracy on the LISS dataset, the model still performs competitively (90.25%), indicating its overall robustness.

To validate the contribution of individual architectural components, we conducted a small ablation study on both datasets. Replacing LW-convMLP UNet with a plain UNet reduced segmentation DSC by 2.8% on LIDC-IDRI and 3.4% on LISS. Removing the LMLP module reduced classification accuracy by 1.9% and increased FPR by 0.006. These results confirm that both the lightweight encoder design and the LMLP-based bottleneck add measurable value to the overall pipeline.

5.4. Discussion

The performance of the proposed LW-convMLP UNet + DRNet-MM framework demonstrates that a lightweight segmentation–classification pipeline can achieve high accuracy across heterogeneous CT datasets. The segmentation results indicate that the combination of LDA-A/LDA-B modules and LMLP blocks enables the model to retain boundary sharpness while remaining computationally efficient. The DRNet-MM classifier, strengthened through patch-level masking and IGJO-based hyperparameter tuning, further enhances benign–malignant discrimination by encouraging the network to learn robust context-aware representations.

An interesting observation is the variation in classification performance across input resolutions. In the LISS dataset, the lower resolution (64 × 64) yielded slightly better results than the 128 × 128 version. This effect can be attributed to the nature of the LISS images, which often contain small, noisy, or low-contrast nodule patterns. Downsampling reduces high-frequency noise and suppresses irrelevant textural variations, enabling the classifier to focus on dominant structural cues. In contrast, LIDC-IDRI contains higher-quality, well-annotated scans where preserving finer spatial detail helps the model identify subtle morphological differences between benign and malignant nodules. This contrast in dataset characteristics explains the differing resolution trends.

The integration of IGJO-based hyperparameter tuning produced consistent improvements across both datasets, particularly in F1-score and sensitivity. Compared with manual tuning, IGJO offered more stable convergence and better exploitation of beneficial parameter combinations, especially under small-data conditions. The ablation results further support the architectural choices: removing the LMLP block or replacing LW-convMLP with a plain UNet resulted in measurable declines in segmentation accuracy and classification performance, confirming the functional contributions of each component.

Overall, the proposed pipeline demonstrates strong potential for deployment in resource-constrained clinical settings, combining efficiency, interpretability, and robust cross-dataset performance. Nevertheless, these findings must be interpreted alongside the methodological limitations outlined below.

5.5. Limitations

This study has the following limitations:

- Dataset Scope: Both LISS and LIDC-IDRI are publicly available datasets with limited patient diversity and imaging variability. These datasets may not fully capture real-world clinical heterogeneity.
- 2D Processing: The framework operates on 2D CT slices rather than full 3D volumes, which may lead to a loss of inter-slice contextual information important for tumor morphology assessment.
- External Validation: The model has not yet been validated on an independent clinical dataset from a hospital or multi-center study. Therefore, generalizability beyond the evaluated datasets remains unproven.
- Ablation Breadth: Although a small ablation was included, more extensive ablation experiments—covering all architectural components and preprocessing steps—could further strengthen the understanding of each module's contribution.

6. Conclusion

There is a growing necessity to identify lung tumors early and classify them to reduce cancer-related fatalities. This study involves preprocessing CT scan images using the RGF and LFE techniques, along with utilizing the LISS and LIDC-IDRI datasets. The DRNet-MM method is employed for sorting, and the study assesses the segmentation performance of the LW-convMLP UNet model in lung cancer (LC). The IGJO algorithm is utilized to optimize the hyperparameters of the model, enhancing the accuracy of the classification model. The study focuses on various metrics in its analysis, including false positive rate (FPR), accuracy, precision, F1 score, sensitivity (SEN), Area Under the Curve (AUC), Dice Similarity Coefficient (DSC), and Jaccard Similarity Coefficient (JSC). With an outstanding precision rating of 99.10% and exceptional accuracy of 99.4% on the LIDC-IDRI dataset, the proposed approach demonstrates clear superiority. Furthermore, the suggested approach achieves a precision of 90.25% and an accuracy of 90.3% for the LISS dataset. These results underscore the superior performance of the proposed method, indicating its effectiveness compared to current methodologies.

In the future, various evolutionary and recommendation models can be employed to enhance predicted performance metrics. Additionally, the creation of hybrid deep learning (DL) models is possible to achieve improved performance metrics in less time.

Authors contribution statement:

Suma K G: Conceptualization, Methodology, Validation
Santhi Gottumukkala: Software, Implementation
Archana Sasi: Conceptualization, Investigation, Writing - review & editing
Santhi Sri T: Writing original draft, Validation.
Ghamya Kotapati: Writing original draft
Ramesh Vatambeti: Methodology, Writing - review & editing
Rama Ganesh B: Methodology, Writing - review & editing

Data availability statement:

The data that support the findings of this study are available upon reasonable request from the authors.

Ethics approval:

The submitted work is original and has not been published elsewhere in any form or language.

Disclosure of potential conflicts of interest:

There is no potential conflict of interest.

Research involving Human Participants and/or Animals: NA

Funding:

The authors declare that no funds, grants, or other support were received during the preparation of this manuscript.

Competing interests: The authors have no relevant financial or non-financial interests to disclose.

References:

1. Sung, H., Ferlay, J., Siegel, R.L., Laversanne, M., Soerjomataram, I., Jemal, A., Bray, F.: Global Cancer Statistics 2020: GLOBOCAN Estimates of Incidence and Mortality Worldwide for 36 Cancers in 185 Countries. CA Cancer J. Clin. 71, 209–249 (2021). https://doi.org/10.3322/caac.21660
2. Riaz, Z., Khan, B., Abdullah, S., Khan, S., Islam, M.S.: Lung Tumor Image Segmentation from Computer Tomography Images Using MobileNetV2 and Transfer Learning. Bioengineering 10(8), 981 (2023). https://doi.org/10.3390/bioengineering10080981
3. Hamza, A., Grimes, M., Boukabou, A. et al. A chaotic variant of the Golden Jackal Optimizer and its application for medical image segmentation. Appl Intell 55, 295 (2025). https://doi.org/10.1007/s10489-024-06084-8
4. Hamed, E.A.R., Salem, M.A.M., Badr, N.L., Tolba, M.F.: An Efficient Combination of Convolutional Neural Network and LightGBM Algorithm for Lung Cancer Histopathology Classification. Diagnostics 13(15), 2469 (2023). https://doi.org/10.3390/diagnostics13152469
5. Shehata, S.A., Toraih, E.A., Ismail, E.A., Hagras, A.M., Elmorsy, E., Fawzy, M.S.: Vaping, Environmental Toxicants Exposure, and Lung Cancer Risk. Cancers 15(18), 4525 (2023). https://doi.org/10.3390/cancers15184525
6. Wenhu Liu, Jinhao Sun, Han Li, Yan Wang, Zhaohui Wang, CSEA-Net: A channel–spatial enhanced attention network for lung tumor segmentation on CT images,iScience, Vol. 28, Issue 3, 2025, 111974.
7. Manikandan, T., Devi, B., Helanvidhya, T.: A Computer-Aided Diagnosis System for Lung Cancer Detection with Automatic Region Growing, Multistage Feature Selection and Neural Network Classifier. Int. J. Innov. Technol. Explor. Eng. 9, 409–413 (2019).
8. Silver, A., Ho, C., Ye, Q., Zhang, J., Janzen, I., Li, J., Yuan, R.: Prediction of Disease Progression to Upfront Pembrolizumab Monotherapy in Advanced Non-Small-Cell Lung Cancer with High PD-L1 Expression Using Baseline CT Disease Quantification and Smoking Pack Years. Current Oncology 30(6), 5546-5559 (2023). https://doi.org/10.3390/curroncol300605546
9. [9] d'Abadie, P., Gheysens, O., Lhommel, R., Jamar, F., Kirchgesner, T., Mazzeo, F., Schubert, T.: Diagnostic Superiority of Dual-Time Point [18F] FDG PET/CT to Differentiate Malignant from Benign Soft Tissue Tumors. Diagnostics 13(20), 3202 (2023). https://doi.org/10.3390/diagnostics13203202
10. [10] Grapatsas, K., Menghesha, H., Dörr, F., Baldes, N., Schuler, M., Stuschke, M., Bölükbas, S.: Pneumonectomy for Primary Lung Tumors and Pulmonary Metastases: A Comprehensive Study of Postoperative Morbidity, Early Mortality, and Preoperative Clinical Prognostic Factors. Current Oncology 30(11), 9458-9474 (2023). https://doi.org/10.3390/curroncol30110458
11. [11] VR, N., Chandra SS, V.: ExtRanFS: An Automated Lung Cancer Malignancy Detection System Using Extremely Randomized Feature Selector. Diagnostics 13(13), 2206 (2023). https://doi.org/10.3390/diagnostics13132206
12. Hiraman A, Viriri S and Gwetu M (2024) Lung tumor segmentation: a review of the state of the art. Front. Comput. Sci. 6:1423693. doi: 10.3389/fcomp.2024.1423693
13. Cellina, M., Cè, M., Khenkina, N., Sinichich, P., Cervelli, M., Poggi, V., Boemi, S., Ierardi, A.M., Carrafiello, G.: Artificial Intelligence in the Era of Precision Oncological Imaging. Technol. Cancer Res. Treat. 21, 15330338221141793 (2022). https://doi.org/10.1177/15330338221141793
14. Maqsood, A., Farid, M.S., Khan, M.H., Grzegorzek, M.: Deep Malaria Parasite Detection in Thin Blood Smear Microscopic Images. Appl. Sci. 11, 2284 (2021). https://doi.org/10.3390/app11052284
15. Said, Y., Alsheikhy, A.A., Shawly, T., Lahza, H.: Medical image segmentation for lung cancer diagnosis based on deep learning architectures. Diagnostics 13(3), 546 (2023). https://doi.org/10.3390/diagnostics13030546
16. Thanoon, M.A., Zulkifley, M.A., Mohd Zainuri, M.A.A., Abdani, S.R.: A Review of Deep Learning Techniques for Lung Cancer Screening and Diagnosis Based on CT Images. Diagnostics 13(16), 2617 (2023). https://doi.org/10.3390/diagnostics13162617
17. Tyagi, S., Talbar, S.N.: LCSCNet: A multi-level approach for lung cancer stage classification using 3D dense convolutional neural networks with concurrent squeeze-and-excitation module. Biomed. Signal Process. Control 80, 104391 (2023). https://doi.org/10.1016/j.bspc.2022.104391
18. Irshad, R.R., Hussain, S., Sohail, S.S., Zamani, A.S., Madsen, D.Ø., Alattab, A.A., Alsaiari, O.A.S.: A Novel IoT-Enabled Healthcare Monitoring Framework and Improved Grey Wolf Optimization Algorithm-Based Deep Convolution Neural Network Model for Early Diagnosis of Lung Cancer. Sensors 23(6), 2932 (2023). https://doi.org/10.3390/s23062932
19. [19] Sun, R., Pang, Y., Li, W.: Efficient Lung Cancer Image Classification and Segmentation Algorithm Based on an Improved Swin Transformer. Electronics 12(4), 1024 (2023). https://doi.org/10.3390/electronics12041024

20. Appadurai, J.P., Prabhu Kavin, B., Lai, W.C.: Multi-Process Remora Enhanced Hyperparameters of Convolutional Neural Network for Lung Cancer Prediction. Biomedicines 11(3), 679 (2023). https://doi.org/10.3390/biomedicines11030679
21. Siddiqui, E.A., Chaurasia, V., Shandilya, M.: Detection and classification of lung cancer computed tomography images using a novel improved deep belief network with Gabor filters. Chemometr. Intell. Lab. Syst. 235, 104763 (2023). https://doi.org/10.1016/j.chemolab.2023.104763
22. Subashchandrabose, U., John, R., Anbazhagu, U.V., Venkatesan, V.K., Thyluru Ramakrishna, M.: Ensemble Federated Learning Approach for Diagnostics of Multi-Order Lung Cancer. Diagnostics 13(19), 3053 (2023). https://doi.org/10.3390/diagnostics13193053
23. Usman, M., Shin, Y.G.: DEHA-Net: A Dual-Encoder-Based Hard Attention Network with an Adaptive ROI Mechanism for Lung Nodule Segmentation. Sensors 23(4), 1989 (2023). https://doi.org/10.3390/s23041989
24. Said, Y., Alsheikhy, A.A., Shawly, T., Lahza, H.: Medical image segmentation for lung cancer diagnosis based on deep learning architectures. Diagnostics 13(3), 546 (2023). https://doi.org/10.3390/diagnostics13030546
25. Ji, Z., Zhao, J., Liu, J., Zeng, X., Zhang, H., Zhang, X., Ganchev, I.: ELCT-YOLO: An Efficient One-Stage Model for Automatic Lung Tumor Detection Based on CT Images. Mathematics 11(10), 2344 (2023). https://doi.org/10.3390/math11102344
26. Zhang, X., Kong, S., Han, Y., Xie, B., Liu, C.: Lung Nodule CT Image Segmentation Model Based on Multiscale Dense Residual Neural Network. Mathematics 11(6), 1363 (2023). https://doi.org/10.3390/math11061363
27. Lanjewar, M.G., Panchbhai, K.G., Charanarur, P.: Lung cancer detection from CT scans using modified DenseNet with feature selection methods and ML classifiers. Expert Syst. Appl. 224, 119961 (2023). https://doi.org/10.1016/j.eswa.2022.119961
28. Shah, A.A., Malik, H.A.M., Muhammad, A., Alourani, A., Butt, Z.A.: Deep learning ensemble 2D CNN approach towards the detection of lung cancer. Sci. Rep. 13(1), 2987 (2023). https://doi.org/10.1038/s41598-022-03740-w
29. Maleki, N., Niaki, S.T.A.: An intelligent algorithm for lung cancer diagnosis using extracted features from Computerized Tomography images. Healthc. Analytics 3, 100150 (2023). https://doi.org/10.1016/j.hcan.2023.100150
30. [30] Bishnoi, V., Goel, N.: Tensor-RT-Based Transfer Learning Model for Lung Cancer Classification. J. Digit. Imaging 1-12 (2023). https://doi.org/10.1007/s10278-023-00752-x
31. Hussain, M., Chen, C., Hussain, M. et al. Optimised knowledge distillation for efficient social media emotion recognition using DistilBERT and ALBERT. Sci Rep 15, 30104 (2025). https://doi.org/10.1038/s41598-025-16001-9
32. Hussain Ali, Y., Sabu Chooralil, V., Balasubramanian, K., Manyam, R.R., Kidambi Raju, S., T. Sadiq, A., Farhan, A.K.: Optimization system based on convolutional neural network and internet of medical things for early diagnosis of lung cancer. Bioengineering 10(3), 320 (2023). https://doi.org/10.3390/bioengineering10030320
33. Dong, Y., Li, X., Yang, Y., Wang, M., Gao, B.: A Synthesizing Semantic Characteristics Lung Nodules Classification Method Based on 3D Convolutional Neural Network. Bioengineering 10(11), 1245 (2023). https://doi.org/10.3390/bioengineering101101245
34. M. Hussain, W. Sharif, M. R. Faheem, Y. Alsarhan, and H. A. Elsalamony, "Cross-Platform Hate Speech Detection Using an Attention-Enhanced BiLSTM Model", Eng. Technol. Appl. Sci. Res., vol. 15, no. 6, pp. 29779–29786, Dec. 2025.
35. Goyal, B., Dogra, A.: Multi-modality image fusion for medical assistive technology management based on hybrid domain filtering. Expert Syst. Appl. 209, 118283 (2022). https://doi.org/10.1016/j.eswa.2020.118283
36. Prema, G., Arivazhagan, S.: Infrared and visible image fusion via multi-scale multi-layer rolling guidance filter. Pattern Anal. Appl. 25, 933–950 (2022). https://doi.org/10.1007/s10044-021-01089-7
37. Chen, J., Zhang, L.: A novel medical image fusion method based on rolling guidance filtering. Internet Things 14, 100172 (2021). https://doi.org/10.1016/j.iot.2021.100172
38. Lin, Y., Cao, D., Zhou, X.: Adaptive infrared and visible image fusion method by using rolling guidance filter and saliency detection. Optik 262, 169218 (2022). https://doi.org/10.1016/j.ijleo.2021.169218
39. Cattani, C.: Cantor Waves for Signorini Hyperelastic Materials with Cylindrical Symmetry. Axioms 9, 22 (2020). https://doi.org/10.3390/axioms9010022
40. Zhang, S., Niu, Y.: LcmUNet: A Lightweight Network Combining CNN and MLP for Real-Time Medical Image Segmentation. Bioengineering 10(6), 712 (2023). https://doi.org/10.3390/bioengineering10060712
41. [39] Huang, K., Yang, J., Liu, H., Hu, P.: Deep learning of radio frequency fingerprints from limited samples by masked autoencoding. IEEE Wirel. Commun. Lett. Early Access (2022). https://doi.org/10.1109/LWC.2022.3198802

42. Xie, Z., Zhang, Z., Cao, Y., Lin, Y., Bao, J., Yao, Z., Dai, Q., Hu, H.: SimMIM: A simple framework for masked image modeling. In Proceedings of the 2022 IEEE/CVF Conference on Computer Vision and Pattern Recognition (CVPR), New Orleans, LA, USA, 18–24 June 2022; pp. 9643–9653. https://doi.org/10.1109/CVPR.2022.01017
43. Chopra, N., Ansari, M.M.: Golden jackal optimization: A novel nature-inspired optimizer for engineering applications. Expert Syst. Appl. 198, 116924 (2022). https://doi.org/10.1016/j.eswa.2022.116924
44. Abualigah, L., Diabat, A., Zitar, R.A.: Orthogonal Learning Rosenbrock's Direct Rotation with the Gazelle Optimization Algorithm for Global Optimization. Mathematics 10, 4509 (2022). https://doi.org/10.3390/math10184509